Aromatization of Ketones over Zeolite Catalysts

Jochem J. B. van Duin

Daily supervisor: Egor Fufachev, MSc

First examiner: Prof. dr. Pieter Bruijnincx

Second examiner: Dr. Gareth Whiting

Inorganic Chemistry and Catalysis

Utrecht University

March 2018

Universiteit Utrecht

Abstract

The aromatization reaction of 4-heptanone over ZSM-5 was studied. 450 °C was found to be the optimum temperature for BTEX (benzene, toluene, ethylbenzene and (para-, meta-, ortho-) xylene) formation. With 29 $\%_c$ yield to BTEX, a Si/Al of 25 was determined to be the optimal ratio. A significant percentage of the carbon did however end up in short chain olefins and C_{5+} aliphatics. Gallium was incorporated in the zeolite framework as a dehydrogenating specie in 1.5, 3 and 4.5 wt.%. Ammonia desorption and pyridine adsorption showed 3 wt.% of Ga having the highest acid site density, and hydrogen reduction showed 3 wt.% Ga having the highest density of active dehydrogenating species. Usage of this catalyst resulted in a BTEX yield of 66 $\%_c$.

Contents

List of Abbreviations

BAS	Brønsted acid site
BET	Brunauer-Emmett-Teller
BJH	Barrett-Joyner-Halenda
BTEX	Benzene, toluene, ethylbenzene and xylenes
EDX	Energy dispersive X-ray spectroscopy
LAS	Lewis acid site
MTL	Mass transfer limitations
Py-IR	Pyridine desorption monitored by infrared spectroscopy
(S)TEM	(Scanning) transmission electron microscopy
TCD	Thermal conductivity detector
TOS	Time on stream
TPD-NH_3	Temperature programmed desorption of ammonia
TPR	Temperature programmed reduction
TSE	Tensile strength effect
VFAs	Volatile fatty acids

1 Introduction

Throughout the years, the demand of chemicals has increased. [1] The main part of the chemicals we use to create e.g. fuel and plastics is created from fossil fuels. These global fossil fuel reserves are however decreasing and at some point the reserves will be depleted. To postpone this depletion as far as possible, or to prevent it from happening in the first place, alternative sources for our chemicals have to be found.

A possible source is biomass, accounting for green chemicals. Chemicals can for example already be created from feedstock such as corn and starch. These bio-based chemicals are denoted as first generation and consist mainly of bioethanol and biodiesel. [2,3] A more abundant feedstock is non-edible materials such as lignin and hemicellulose. The products of conversion of these molecules are for example sugars and fuels, and is referred to as second-generation bio-based chemicals. [2,3]

Another possible source of chemicals is produced constantly at plants all around the world, wastewater. Wastewater contains many resources, which can be converted to valuable green chemicals. Optimization of this process could result in a greener industry.

The main interest of this project lies with glucose-rich wastewater from for example the paper-industry.[4] Glucose can be fermented to form volatile fatty acids (VFAs) by the reaction mechanism shown in **Figure 1** [5] under the exclusion of carbon dioxide and hydrogen.[6] The fermentation reactions take place inside different strains of bacteria. The most relevant reactions are the production of acetic-, propionic- and butyric acid, which occur in different strains of the Acetobacter,[7] Proprionibacterium,[8] and Butyricum[5] respectively. The fermentation broth does however contain multiple metal salts and trace elements, which could act as poison for the catalyst. [9]

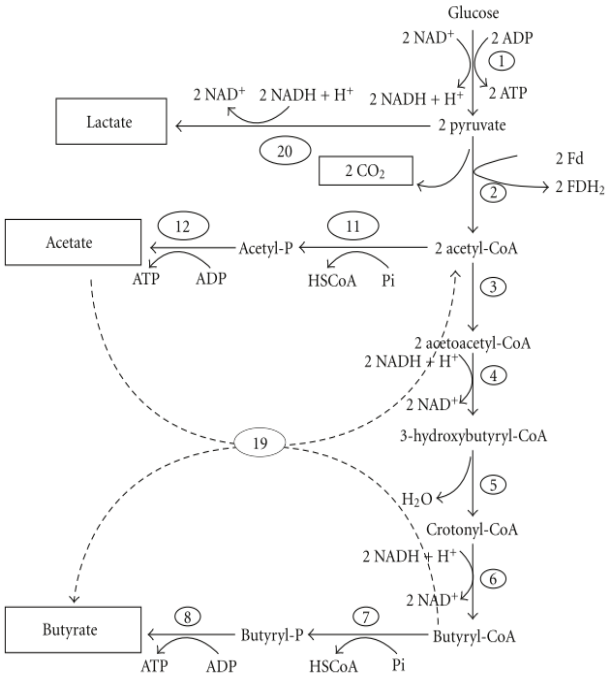

Figure 1 Fermentation of glucose to VFAs.[5]

VFAs can be extracted from the fermentation broth by use of non-functionalized polystyrene-divinylbenzene-based resins.[10] Per kg of adsorbent approximately 60.7 grams of butyric-, 13.3 grams of propionic-, and 1.5 grams of acetic acid is desorbed. The resin still runs at full capacity after 4 desorption cycles, indicating a stable extraction method[10]

The resulting VFAs can be upgraded by ketonization. Two acids can react over amphoteric metal oxides to form ketones under the exclusion of CO_2 and water.[11] During the ketonization of the acids mixture both asymmetric ketones (formed via cross-ketonization) together with symmetric ketones (via homo-ketonization) can be formed. The ketonization of acetic acid has been described in literature manifold.[12,13] However, the statistical product distribution of the ketonization of mixed acids is depicted in **Figure 2,** with 4-heptanone as the largest component in the products.[14]

Ketones are valuable platform chemicals, but a final valorisation can take place by aromatization. Aromatics are of great interest of the (petro) chemical industry, and within those aromatics the main interest lies with benzene, toluene, ethylbenzene and (*ortho-, meta- and para-*) xylene (BTEX). BTEX is used for the creation of a large variety of polymers such as polystyrene (PS) and polyethylene terephthalate (PET).[15,16] Since 4-heptanone is the most abundant product in the ketonization of VFAs, the main objective in this thesis lies with the aromatization of 4-heptanone. This aromatization of hydrocarbons can be catalysed by acidic materials.[17]

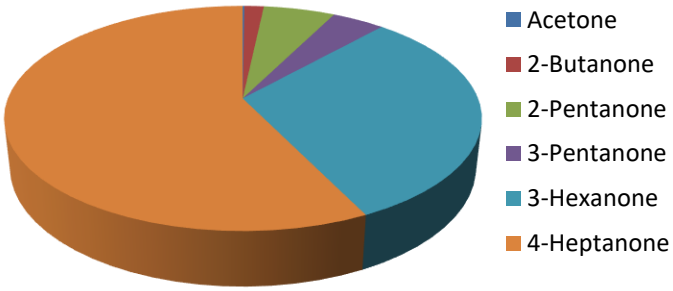

Figure 2 Product distribution of the reaction of the extracted VFAs over titania.

2 Theory

2.1 Catalyst

2.1.1 Zeolites

Acid sites are required to catalyze the aromatization reaction.[17] One of the most readily available groups of solid acidic materials are zeolites. Zeolites are highly ordered microporous aluminosilicate materials. The main benefit of this microporosity is the prevention of forming large, polyaromatic, molecules. In an optimal catalyst monoaromatics would fit through the pores, but larger compounds will be prevent from being formed due to size constraints.[18] One of the commercially available zeolites with small pore size is Zeolite Socony Mobil-5 (ZSM-5). The pores of ZSM-5 consist of a 10-membered ring with a diameter of approximately 5.6 Å. This diameter should be sufficient for the formation of monoaromatics,[19] and at the same time narrow enough to prevent polyaromatic formation.[20]

Aluminium atoms in the framework create the acid sites in zeolites. An aluminium atom can either be at a tetrahedral position, resulting in a negative charge on the aluminium, which can be countered by a proton, causing a Brønsted acid site (BAS). Alternatively, an aluminium atom can be at a trigonal position, with a neighbouring trigonally bonded silicon atom. As a result the silicon will carry a positive charge and act as an electron pair acceptor, creating a Lewis acid site (LAS), as depicted in **Figure 3**.[21–23] Since all acid sites are created surrounding an aluminium atom, the amount of acid sites in a zeolite can be expressed by use of the silicon to aluminium ratio (Si/Al). The strength of the acid sites can also be influenced by this Si/Al. The strongest acid sites occur when the next nearest neighbours (NNN) of the aluminium atom are all silicon atoms. Resulting in an increasing acid strength upon decreasing Si/Al.[24,25] As mentioned before, due to the small pore sizes of zeolites larger hydrocarbons such as polyaromatics are not able to leave the pores. These large, inactive hydrocarbons are referred to as coke. [26] These coke molecules block the pores and acid sites, and thus the active sites, of the zeolite. Regeneration of the catalyst is possible by burning the coke at elevated temperatures. [27]

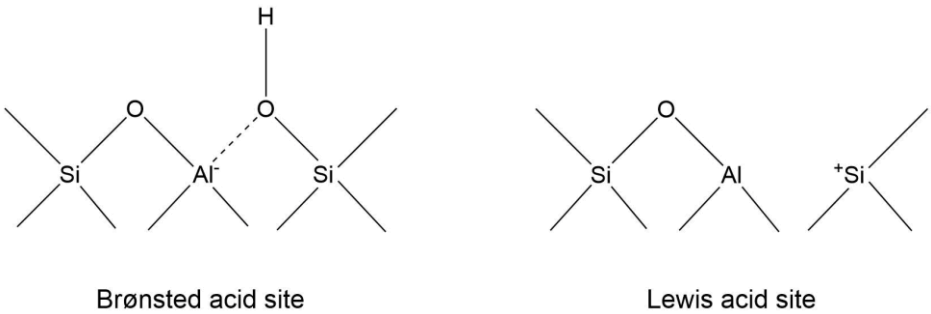

Figure 3 Nature of Brønsted and Lewis acid sites in zeolite materials. [23]

2.1.2 Metal doping

Besides acidic sites, presence of dehydrogenating sites positively influence the aromatization abilities of the catalyst. These sites can be implemented by incorporation of metals such as Pt, Zn and Ga.[17] The metals can be incorporated by the use of different techniques such as ion exchange, chemical layer deposition and wet impregnation.[28] Gallium impregnation on zeolites has already shown to be of great influence on the aromatization of propane.[29] The gallium occurs in three distinct forms: well dispersed Ga_2O_3, GaO^+ and segregated bulk Ga_2O_3. Among these states, GaO^+ is reported to be the active species for hydrocarbon dehydrogenation.[30] These species should result in an increase in LAS on the zeolite. [31]

2.2 Aromatization over zeolites

Since the aromatization over zeolite catalysts has been reported in literature manifold, a small overview on the literature of aromatization and mechanisms of ketone-like materials are shown below.

2.2.1 Paraffins and olefins

Due to the possibilities of using liquefied petroleum gas (LPG) as a feedstock for aromatic production, much research has been performed on the formation of BTEX from short chain paraffins of which mainly propane is a compound of interest.[17] The initial step of the paraffin aromatization reaction is the formation of olefins. Propane can either be dehydrogenated to obtain propylene and H_2, or be cracked to obtain methane and ethylene.[27,32]

The aromatization of olefins is depicted in **figure 4** [17] where D indicates dehydrogenating sites, which are either acidic sites or metal sites. Whereas A indicates that the reaction takes place over acid sites provided by the zeolite material. Olefins are oligomerized on these acid sites, forming longer chain alkenes. These C_{6+} alkenes are converted to dienes either by dehydrogenating metal sites, or by hydrogen transfer from long chain and cyclic olefins to short chain alkenes. Longer paraffins such as n-heptane follow a similar reaction path, but are dehydrogenated directly to C_6-C_{10} alkenes.[33]

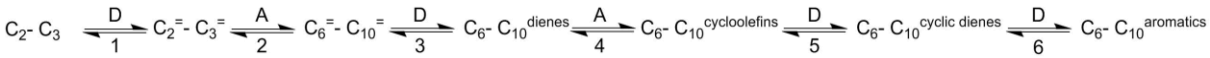

Figure 4 Reaction pathway on the aromatization of short chain paraffins. D indicates a dehydrogenating site and A indicates an acid site. [17]

2.2.2 Alcohols

The methanol to gasoline (MTG) process was already reported and pilot-scale used by Mobil in 1977 [34,35], but interest in the process was regained with the recent developments in "green methanol".[36] The proposed reaction scheme is depicted in **figure 5**[37] where first one methanol molecule is bound to a BAS and reacts with a second methanol molecule to form dimethyl ether (DME).[38,39] DME can subsequently react to olefins under the exclusion of water. The resulting olefins can in turn either undergo another methylation reaction, forming higher olefins, or undergo the process depicted in Figure 4 to form aromatics. [40,41]

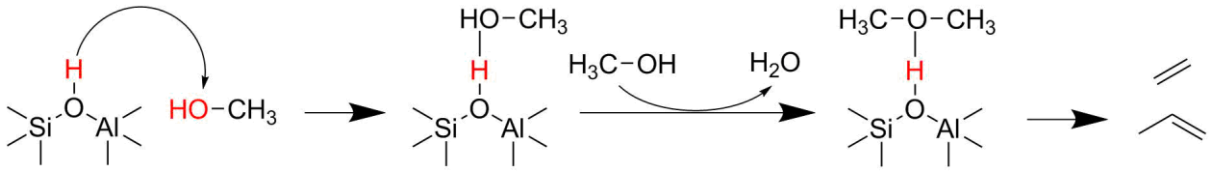

Figure 5 Aromatization of methanol over zeolites. [37]

2.2.3 Aldehydes

Another group of chemicals created from biomass is aldehydes. Aldehydes are present in biomass pyrolysis oil.[42,43] Among aldehydes mainly propanal is a compound of interest for aromatic production. The reaction of propanal over ZSM-5 realizes monoaromatic yields up to 50 %.[44] This aromatization occurs in several ways. One of the options is the dehydrogenation or cracking where short chain paraffins and olefins are formed, which can in turn be converted to aromatics as depicted in Figure 4. The second reaction path is an aldol condensation trimerization followed by cyclization, depicted in **Figure 6**. The trimerization of propanol creates 1,3,5-trimethylbenzene under the exclusion of water.[45] Subsequently trimethylbenzene can be dealkylated on ZSM-5, forming BTEX molecules and short chain hydrocarbons. [46]

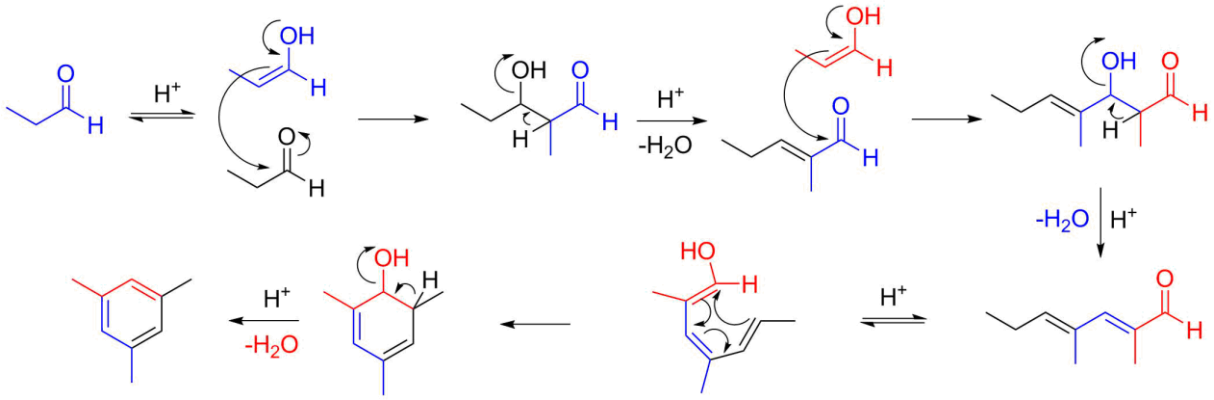

Figure 6 Propanal to aromatics through aldol trimerization. [45]

2.2.4 Ketones to Aromatics

Throughout the years, some research has been done on the aromatization of ketones. The focus lies with the aromatization of acetone. The first reported results on the aromatization of acetone over ZSM-5 was by Nedomová et al.[47] where acetone was reacted with a weight hourly space velocity (WHSV) of 11.7 h^{-1} at 300 and 350 °C and a Si/Al of 16.6. Realizing an optimum conversion of 41.7 % with an aromatic selectivity of 29.7 %. During these experiments no suggestions on the reaction path were given.

Setiadi et al. looked into the effect of higher temperatures and a variable space velocity on the aromatization of acetone over ZSM-5 Si/Al 25. They report that increasing the temperature to 400 °C ensures nearly full conversion of acetone.[48] At this full conversion the space velocity influences the product distribution significantly. Out of the tested space velocities (2.18, 4.74 and 7.13 h^{-1}) the lowest WHSV of 2.18 h^{-1} is reported to show the highest selectivity to BTEX of 54 $\%_c$.

Variation of the Si/Al at these conditions were later tested by Slamet et al.[49] ZSM-5 with Si/Al of 25, 75 and 100 were used for the aromatization of acetone at 400 °C and a WHSV of 4 h^{-1}. The catalysts were tested up to 10 hours on stream. During this reaction ZSM-5 with Si/Al 25 shows a negligible change in conversion of acetone, while Si/Al 75 and 100 have lost 40 % of their activity after 10 hours.[49]

Gayubo et al. reported that acetone conversion over ZSM-5 at 400 °C leads to the formation of some i-butene, and proposed it to be the first step in the aromatization of acetone.[50] The proposed aromatization pathway is depicted in **Figure 7**, where aromatics and C_{4+} paraffins are the main products at low space velocities.[50] Gayubo et al. report that increasing the WHSV above 1.25 results in an increased formation of propene and decreased selectivity towards aromatics.

The main focus of this thesis is however the conversion of 4-heptanone to aromatics. Little is known about this aromatization reaction. Fuhse et al. briefly touched the subject by stating that a BTEX yield of 39 wt.% can be achieved with a weight hourly space velocity (WHSV) of 0.49 h^{-1} and a reactor temperature of 400 °C. [51] There is however no data available on the use of different conditions for the reaction of 4-heptanone, nor is there a mechanism proposed in literature.

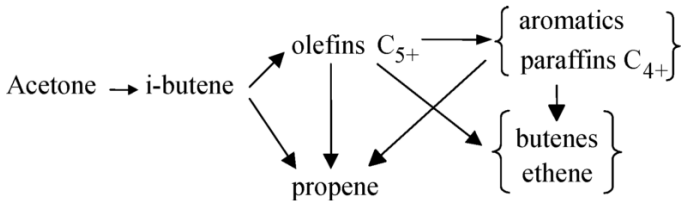

Figure 7 Aromatization path of acetone over ZSM-5. [50]

3 Methodology

3.1 Catalyst Preparation

3.1.1 Commercial ZSM-5

Commercial ZSM-5 (Zeolyst, NH_4-ZSM-5) with Si/Al of 11.5, 25, 40 and 140 were used. The catalysts were converted to their protonated form by calcining at 700 °C for 6 hours in stagnant air with a temperature ramp of 5 °C/min.

3.1.2 Ga-ZSM-5

Ga-doped ZSM-5 was prepared by wet impregnation. The synthesis procedure was as following: one gram of HZSM-5 with a Si/Al of 25 was crushed and dried at 120 °C for 2 hours. Afterwards the solid was dispersed in 50 mL of MilliQ water (18,2 MΩ·cm at 25 ^{o}C) and stirred at 500 rpm for 30 minutes. An aqueous solution of $Ga(NO_3)_3 \cdot xH_2O$ (Acros Organics, 99.9998 % trace metal basis), was added to the mixture, to obtain a 3 wt.% gallium loading. The stirring was maintained for 3 hours. Afterwards the water was removed by the use of rotation evaporation. The resulting catalyst was dried overnight at 120 °C followed by calcination at 550 °C for 5.5 hours with a temperature ramp of 5 °C/min. The resulting material was denoted as 3%Ga-ZSM-5

Ga-doped zeolites with a loading of 1.5 wt.% and 4.5 wt.% were synthesised following the same procedure. The catalysts were denoted as 1.5%Ga-ZSM-5 and 4.5%Ga-ZSM-5 respectively.

3.1.3 Pore Modified ZSM-5

Pore-modified ZSM-5 was synthesised by chemical liquid deposition (CLD) as reported by Zheng et al.[52] 2g of H-ZSM-5 with a Si/Al of 25 was crushed by pestle and mortar and dispersed in 50 mL of mixed hexanes (Interchema, 98%). 0.30 mL of TEOS (Aldrich, ≥99) was added to the mixture, to obtain a SiO_2 loading of 4 wt.%. The mixture was refluxed at 90 °C for 1 h during continuous stirring at 500 rpm. The catalyst was separated by centrifugation and subsequently dried in static air at 100 °C for 2 h. Finally, the catalyst was calcined for 4 h at 500 °C in static air with a temperature ramp of 5 °C/min. The procedure was repeated twice more to end up with a final SiO_2 loading of 12 wt.% The resulting catalyst is denoted as PMM-ZSM-5.

3.1.4 Pore Modified Ga Doped ZSM-5

Gallium doped pore modified ZSM-5 was synthesised by depositing 3 wt.% Ga on PMM-ZSM-5 in the manner described in **§3.1.2**. The resulting material was denoted Ga-PMM-ZSM-5.

3.2 Characterization Techniques

3.2.1 Physisorption

The surface areas of all catalytic materials were measured using Ar-physisorption on the Micrometrics TriStar Analyzer V6.08. Prior to the measurement the samples were dried under low pressure (10 mbar) at 400 °C for 16 hours. The physisorption was performed at 77 K.

3.2.2 X-Ray Diffraction

X-ray measurements were performed on a Bruker D2, with a cobalt X-ray source (λ (Kα) =1.79026 Å). All samples were measured in the range of 7 ° > 2θ > 50 ° with an increment of 0.028 °/s. The crystal phases were determined using the PDF 2015 database.

3.2.3 Temperature Programmed Desorption

The amount of acid sites was measured using temperature programmed desorption of NH_3 (TPD-NH_3). The measurements were performed on a Micrometrics Autochem II analyzer equipped with a Thermal Conductivity Detector (TCD). 100 mg of sample was loaded in a quartz reactor and dried at 650 °C for 15 minutes, with a temperature ramp of 10 °C/min. After cooling to 100 °C the sample was saturated using 20 pulses of 10% NH_3 in He. After the saturation the sample was equilibrated at 100 °C for 1 h and heated to 650 °C with a temperature ramp of 5 °C/min.

3.2.4 Temperature Programmed Reduction

The oxidation states of doped materials were measured using temperature programmed reduction with H_2 (H_2-TPR). The sample was dried for 1 h at 450 °C. Consecutively the sample was cooled to room temperature, and the atmosphere switched to a 5% H_2 in He. The sample was heated to 1000 °C with a rate of 5 °C/min under a 5% H_2 in He flow. The measurement was performed on a Micrometrics Autochem II analyser equipped with a TCD.

3.2.5 Pyridine Adsorption FT-IR

The nature of the acid sites on the catalysts were measured by the temperature programmed desorption of pyridine monitored by infrared spectroscopy (Py-IR). The IR spectra were recorded on the Thermo IS5 spectrometer. For each spectrum, 32 scans were recorded with a resolution of 4.0 cm^{-1}. Self-supporting pellets of approximately 15 mg sample with a diameter of 12 mm were made by crushing the sample and pressurizing it at approximately 0.6 GN/m^2 for 30 s. The catalysts were dried at 550 °C under ultra-high vacuum (UHV, 10^{-7}-10^{-9} mbar) for 30 minutes. The sample was cooled to RT and pyridine was adsorbed to the sample at 10-20 mbar for the duration of 35 minutes. Pyridine was desorbed in the temperature range of 50 – 550 °C under UHV with a temperature ramp of 10 °C/min. 550 °C was maintained for 30 minutes to ensure complete desorption of pyridine.

3.2.6 Transmission Electron Microscopy/Energy Dispersive X-ray Spectroscopy

TEM samples were prepared by addition of 0.1 mL iso-propanol (Sigma Aldrich, ≥99.5%) to 5 mg of catalyst. The resulting mixture was dispersed in an ultrasonic bath for 10 minutes and one droplet of the mixture was dripped on a carbon coated formvar TEM grid, mesh 300. The samples were measured on the Philips FEI Tecnai F20 S/TEM equipped with a 200kV field emission electron gun (S/TEM) and on a Fei Talos F200X (S)TEM, equipped with an XFEF 200kV electron gun (S/TEM and EDX).

3.2.7 GC x GC-QP-MS

Products of the reaction were condensed by use of a liquid nitrogen trap. GC x GC-QP-MS samples were prepared by dissolving the condensed products in deuterated chloroform (Euriso-top, ≥99.8 %). The samples were stored at -20 °C.

GC x GC-QP-MS analysis was carried out on a Shimadzu GCMS-QP2010 Ultra equipped with a Zoex ZX 1 modulator. The columns are a low polarity/medium polarity set placed in a single oven. The specifics of the columns are given in **Table 1**.

Table 1 GC x GC-QP-MS column set specifics.

Position	Model	Polarity	Dimension (m x mm x mm)
Primary	Agilent VF-5ms	Low	30 x 0.25 x 0.25
Secondary	Agilent VF-17ms	Medium	2 x 0.15 x 0.15

3.3 Catalytic testing

Catalytic tests were performed in a fixed bed reactor depicted in **Figure 8**. The liquid reactant (4-heptanone (Alfa Aesar, 98%) or a mixture of acetic- propionic- and butyric acid) was fed using a Shimadzu LC-20AT liquid chromatograph in various space velocities. The liquid reactant was evaporated in a Swagelok 304L stainless steel sample cylinder, which was heat-traced to 180 °C. The reactions take place in a quartz reactor placed in an oven with a variable temperature of 300 - 450 °C. In order to minimalize temperature gradients inside the catalytic bed, the catalyst was mixed with silicon carbide (SiC, Acros, Technical grade) in a 2 : 1 v : v ratio of SiC to catalyst. The catalytic bed was fixed between two layers of 200 mg of SiC and quartz wool. Nitrogen was used as carrier gas with a flow of 100 mL/min during all reactions. On-line GC (Bruker 430GC) equipped with an Agilent Poraplot Q-HT (25 x 0.32 x 0.32) analytical column was used for quantification of the products. Cyclooctane (Sigma Aldrich, ≥ 99%) was used as an internal standard.

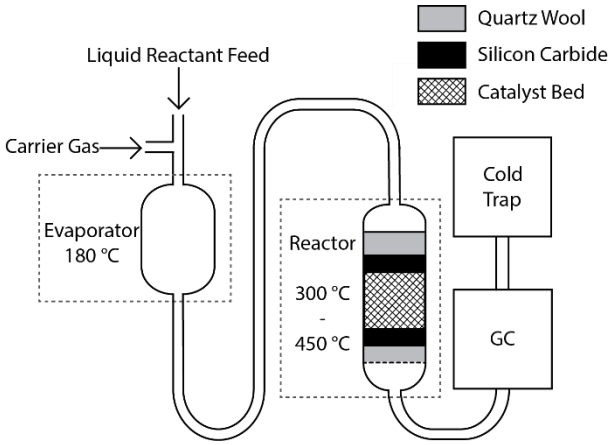

Figure 8 Catalytic testing set-up. All lines were heat traced at 200 °C.

Catalytic testing of the materials with water as stability enhancer was performed by co-feeding of MilliQ water (18,2 MΩ·cm at 25 °C) using a Shimadzu Nexera X2 LC-30AD liquid chromatograph.

4 Results and Discussion

4.1 Catalyst Characterization

4.1.1 Commercial ZSM-5

4.1.1.1 X-Ray Diffraction

Figure 9 shows the powder X-ray diffractograms of ZSM-5 with different Si/Al and the simulated diffractogram of MFI structures.[53] All materials show a similar diffraction pattern corresponding to a monoclinic structure, which is expected for ZSM-5 at room temperature.[54] The difference in detail between the literature and the actual measurements is due to the increment and measuring time.

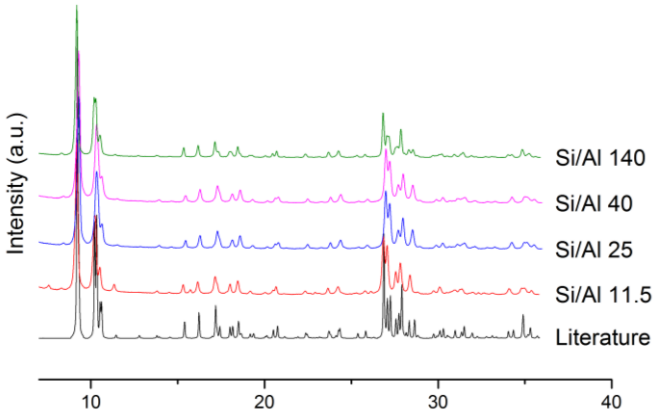

Figure 9 Powder X-ray diffractograms of ZSM-5 with varying Si/Al.

4.1.1.2 Ar-Physisorption

The surface areas of ZSM-5 were measured using Ar-physisorption. Argon was used as the probe molecule because the strong acid sites in zeolites can induce a dipole moment in a nitrogen molecule, resulting in bilayer formation.[55] Brunauer-Emmett-Teller (BET) analysis was performed to calculate the surface area. The surface areas of the different materials are given in **Table 2**. The adsorption-desorption isotherms are shown in Appendix A1. All catalysts show a type H4 hysteresis loop, indicating the filling of micropores, expected to be present in zeolites [56,57]

Furthermore a Barrett-Joyner-Halenda (BJH) analysis was applied to estimate the pore size distribution of the materials. The different plots are depicted in Appendix A2. The BJH-analyses of the zeolite materials show two characteristics. One peak can be observed at 3.7 nm, which can be ascribed to the Tensile Strength Effect (TSE). [55,57] And an increase of pore volume on the left hand side of the desorption plot, indicating that the actual pore size of the material is smaller than 1 nm, which is coherent with the 5.6 Å channels described in literature.[58]

Table 2 Surface areas of the different Si/Al ZSM-5, measured with Ar-physisorption and BET analysis.

Si/Al	BET surface area (m^2/g)
11.5	366
25	468
40	438
140	403

4.1.1.3 TPD-NH_3

The NH_3-desorption profiles are illustrated in Appendix B**.** All materials show two peaks, the nature of these peaks is still debatable since the peak at a lower temperature can be assigned to either weak acid sites, or to physisorbed ammonia on the surface of the zeolite.[59,60] The peak at a higher temperature corresponds to stronger acid sites.

Since, as explained in more detail in §2.1.1, acid sites of zeolites are created either by a tetrahedrally coordinated aluminium atom in the zeolite, or by trigonally bonded silicon and aluminium atoms, an increasing Si/Al should decrease the amount of acid sites in the sample.[21,22] **Figure 10** shows the correlation between the amount of acid sites per surface area and the Si/Al ratio and indicates that, as reported in literature,[21] a decreasing aluminium content does indeed decrease the acid site density.

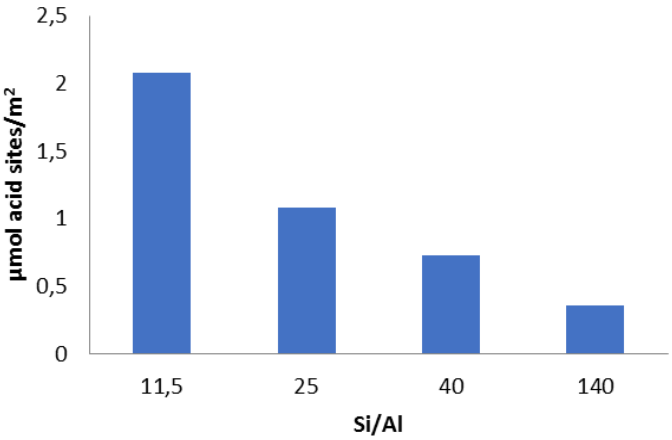

Figure 10 Acid site density on ZSM-5 with varying Si/Al.

4.1.2 Ga-ZSM-5

4.1.2.1 X-Ray Diffraction

The powder diffractograms of Ga-doped catalysts are shown in **Figure 11**. The materials all show similar peaks corresponding to the monoclinic ZSM-5 framework. ZSM-5 with a Ga loading of 3 wt.% shows a small decrease in peak intensity at 2θ values of 11 and 28°. Rietveld refinement using Bruker DIFFRAC.SUITE TOPAS indicates that the sample has a smaller average crystallite size, accounting for the broader, and thus overlapping, peaks. The PDF 2015 database indicates that Gallium oxide peaks are expected to appear at 39 and 42 ° 2θ. The absence of these peaks indicates that the gallium is either amorphous, or the crystallites are too small to show a significant signal in XRD.

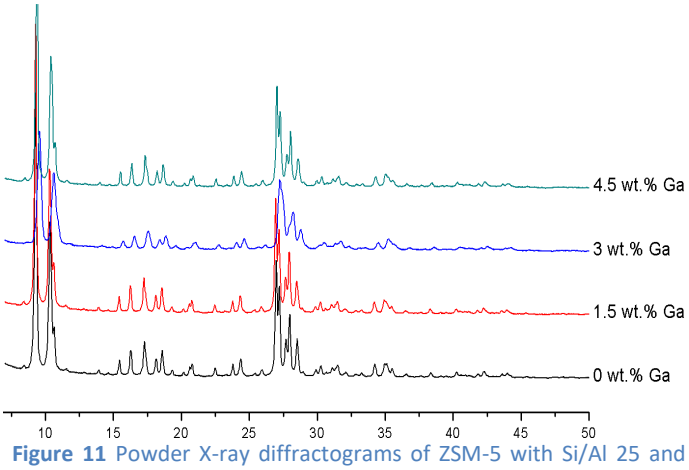

Figure 11 Powder X-ray diffractograms of ZSM-5 with Si/Al 25 and different loadings of Ga.

4.1.2.2 Ar-Physisorption

Argon physisorption measurements of the gallium impregnated samples show little difference in BET surface areas, but do show a noticeable decrease of surface area between the Ga-ZSM-5 and commercial ZSM-5 with surface areas of 415 and 467 m^2/g respectively. This decrease in surface area is most likely due to blockage of some of the micropores by gallium particles. The surface area does not decrease significantly with increasing gallium content. This is most likely due to the formation of more segregated Ga_2O_3 particles upon increasing weight loading, creating extra surface area without closing a significant amount of pores. The BJH analyss of 1.5 and 3 wt.% Ga indicate the presence of just pores below 1 nm in diameter, while 4.5 wt.% Ga-ZSM-5 indicates both pore diameters below 1 nm and pores of approximately 5 nm in diameter as depicted in **Figure 12**. These 5 nm pores are expected to be due to either gaps between segregated Ga_2O_3 particles and the zeolite material or collapsed channels due to the gallium deposition. These collapsed channels would be to a small extend since no significant change in surface area is observed. The other BJH plots and physisorption isotherms can be found in appendix A1.

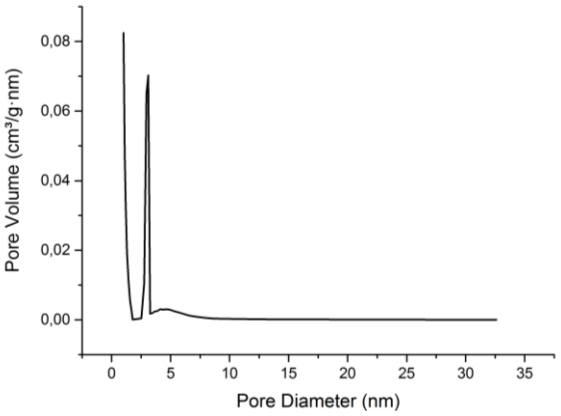

Figure 12 BJH analysis of 4.5%Ga-ZSM-5 Si/Al 25. The analysis indicates the presence of pores of around 5 nm in diameter.

4.1.2.3 H_2-TPR

Gallium impregnated on zeolites knows 3 major forms.[30] The different states of gallium are reduced at different temperatures. Reduction around 500 °C is attributed to small Ga_2O_3 particles in close vicinity of the zeolite,[61] reduction at 650 °C corresponds to the reduction of GaO^+ (III) to Ga^+ (I) incorporated

in the zeolite framework and the peak at 825 °C indicates reduction of segregated bulk Ga_2O_3.[62] **Figure 13** shows the reduction profiles of the different Ga-ZSM-5 samples, the individual profiles and corresponding deconvoluted peaks can be found in Appendix C.

Figure 13 shows that 1.5%Ga-ZSM-5 has small Ga_2O_3 particles on the zeolite, and incorporated GaO^+ particles while 3%Ga-ZSM-5 shows a small increase in the incorporated GaO^+ peak and the presence of some segregated bulk Ga_2O_3. Lastly, the TPR profile of 4.5%Ga-ZSM-5 indicates a big portion of the impregnated gallium in the segregated bulk Ga_2O_3 form. This increase in the 825 °C peak is an indication of a too high gallium content, forming extra crystalline bulk Ga_2O_3. **Table 3** shows an estimation of the wt.% of gallium present in each of the forms on the different sample based on the TPR- profiles. The table indicates that 3 wt.% Ga ZSM-5 has the highest concentration of the active species (GaO^+). Increasing the gallium weight loading further results in the increase of segregated bulk Ga_2O_3.

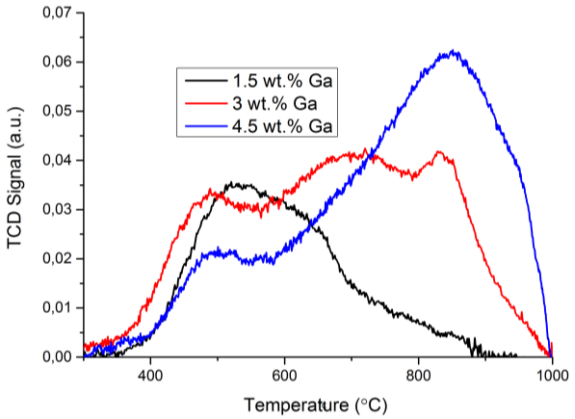

Figure 13 Reduction profiles of 1.5, 3 and 4.5 wt.%Ga ZSM-5 Si/Al 25.

Table 3 weight percentages of gallium in the different phases, determined by H_2-TPR.

Wt. % Ga	1,5	3	4,5
Well dispersed Ga_2O_3	0.70	0.53	0.70
GaO^+	0.59	2.18	1.38
Seggregated bulk Ga_2O_3	0.21	0.29	2.42

4.1.2.4 TPD-NH_3

The amount of acid sites in fresh ZSM-5 Si/Al 25 and gallium-impregnated ZSM-5 were measured using ammonia TPD. The desorption profiles are presented in Appendix B. The total amount of acid sites per m^2 are shown in **Figure 14**. The figure depicts an increasing acid site density upon increasing gallium loading, up until 3 wt.%, whereas a weight loading of 4.5 % gallium shows a decrease in the acid site density. TPD-NH_3 does however give a value for the total acid site density, and can not differentiate between BAS and LAS. For this reason pyridine desorption experiments have been performed to determine the nature of the acid sites.

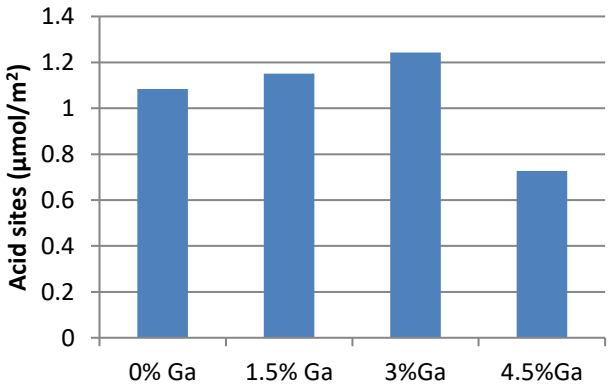

Figure 14 Acid site density upon changing gallium loading by TPD-NH_3.

4.1.2.5 Pyridine FTIR

Pyridine desorption monitored by IR spectroscopy (Py-IR) provides an indication of the type of acid site (Brønsted and Lewis) and could because of this show the effect of Ga-doping on catalysts acidity. Pyridine bound to different acid sites show vibrations at different energies. Pyridine chemisorbed on a LAS vibrates at 1455 cm^{-1}, this vibration is however close to the vibration of physisorbed pyridine at 1437 cm^{-1}.[63] Peaks at 1545 cm^{-1} occur due to the vibration of a pyridinium molecule, indicating pyridine bound to a BAS. [64–67] **Figure 15** shows the IR-spectra of pyridine adsorbed on ZSM-5 during desorption at 150 °C for ZSM-5 Si/Al 25 with different Ga-loadings.

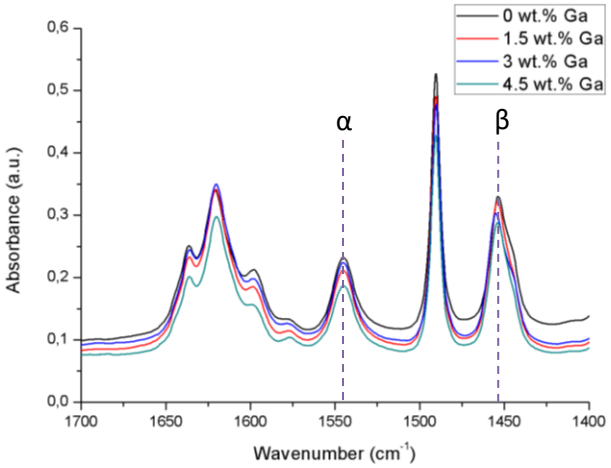

Figure 15 Pyridine desorption spectra at 150 °C on ZSM-5 Si/Al 25 with different Ga loadings. The peak indicated by α corresponds to BAS, and β to LAS.

$$[Acid\ Sites] = \frac{A \times 10^3}{\varepsilon \times \rho} \quad \textbf{(1)}$$

The amount of acid sites can be determined by use of equation 1,[68] where A is the integral of the vibrational band, ρ corresponds to the mass of the sample per cm^2, which is 13.26 g/cm^2 and ε is the extinction coefficient, equal to 1.67 and 2.22 cm/µmol for Bronsted and Lewis acid sites respectively.[69] The density of Lewis- and Brønsted acid sites are shown in **Figure 16**. The figure shows a clear increase of Lewis acid site density with Ga addition. The different loadings do however show a less apparent change. The Lewis acid site density shows a small optimum at the 3 wt.% Ga. The BAS density does not show a clear correlation with changing gallium loading. **Figure 17** shows the total amount of acid sites according to both techniques, first, the difference between acid sites detected on Py-IR and TPD-NH_3 could be due to NH_3 penetrating smaller pores, or physisorbing to the surface. By combining the amount of acid sites with the TPR data from Table 2, it can be concluded that the sample with the highest amount of segregated bulk Ga_2O_3 shows the lowest acid site density. This could be due to the possibilities of surfaces being blocked by the bulk Ga_2O_3 particles. These blocked surfaces do not show a significant decrease of BET surface area, due to the formation of surface area by the bulk Ga_2O_3 particles. Another aspect can be seen in the quantity of acid sites in 3 wt.% Ga-ZSM-5. According to H_2-TPR this sample has the highest quantity of GaO^+, which should create Lewis acid sites. Both techniques also show the highest acid site density for this material.

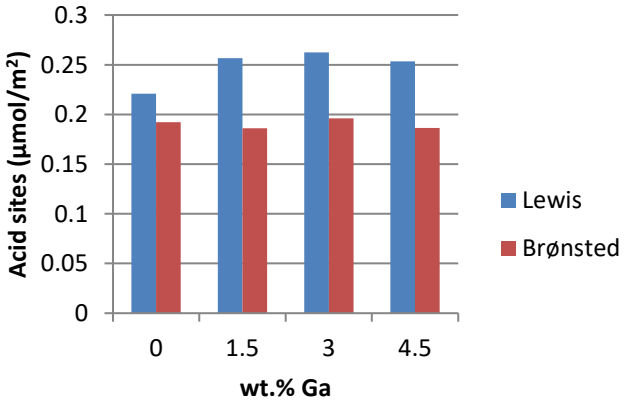

Figure 16 Density of LAS and BAS on different Ga-ZSM-5 samples.

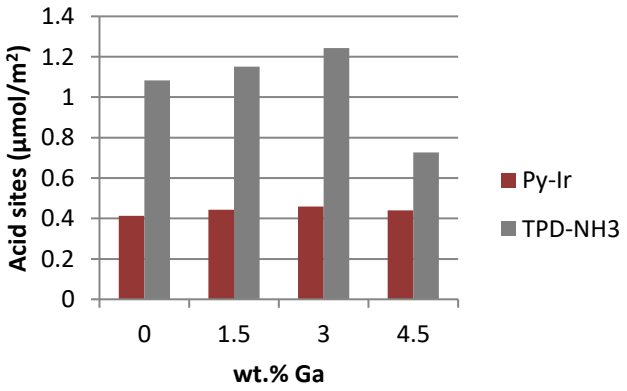

Figure 17 Comparison of the total acid site density according to Py-IR and TPD-NH_3 upon changing gallium loading.

4.1.2.6 TEM/EDX

Figure 18 shows the dark field TEM/EDX images of 3%Ga-ZSM-5. Channels of higher intensity in TEM can be observed in the different images. These channels were concluded to be Ga-rich by the use of field EDX (**Figure 18**). An inhomogeneous distribution of Ga on the zeolite can be seen. The clustering is coherent with the presence of segregated bulk Ga_2O_3 indicated by TPR. And was observed on all samples.

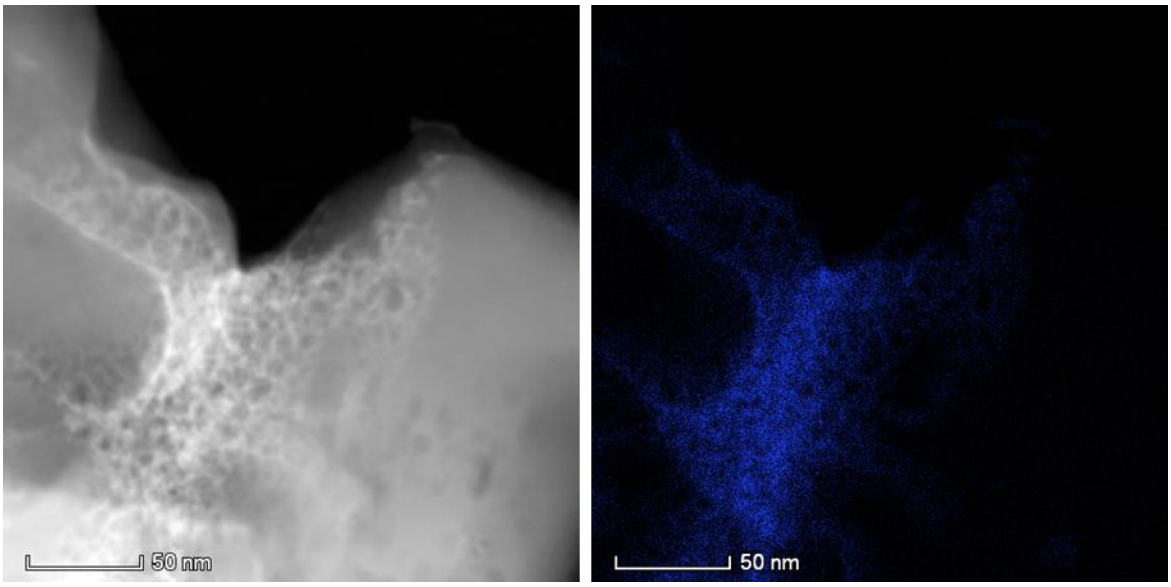

Figure 18 Left: Dark field TEM image of 3%Ga-ZSM-5. Right: Elemental mapping of gallium (blue) on 3%Ga-ZSM-5.

4.2 Conversion of 4-heptanone

4.2.1.1 Mass Transfer Limitations

ZSM-5 has micropores of approximately 5.6 Å,[58] because of this small pore size, internal mass transfer limitation (MTL) is likely to occur. Experimentally this can be checked by a method proposed by Fogler.[70] The reaction rate was studied as function of (Gas velocity/Particle diameter)$^{1/2}$. Increasing the gas velocity or decreasing the particle size leads to an increase in reaction rate if mass transfer limitations are present. In the region where no MTL occur, the reaction rate should remain constant upon changing the gas velocity or particle diameter.[71]

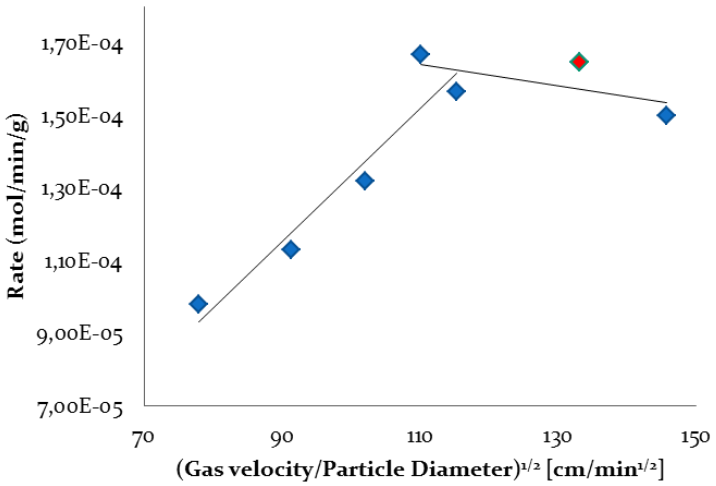

Figure 19 Reaction rate at varying particle size and carrier gas flow during the 4-heptanone to aromatics reaction over ZSM-5.

Aromatization reactions of 4-heptanone over ZSM-5 were performed with various nitrogen flows of 30-125 mL/min and with catalyst particle diameters ranging from 38 to 150 µm. The reaction rates at the different conditions were measured and are depicted in **Figure 19**. The figure shows that a (Gas velocity/particle diameter)$^{1/2}$ of 110 is the breaking point for mass transfer limitations. Below this value, internal MTLs are present, above this value the reaction occurs without internal limitations.

For this reason the reaction tests were performed using catalysts with particle diameters of 38-75 µm and carrier gas flow of 100 mL/min.

A second way to evaluate internal MTL is by use of the Weisz-Prater criterion (**Equation 2**). If the value of the criterion is smaller than or equal to 0.3, no internal diffusion limitations are present. [72]

$$N_{W-P} = \frac{\Re R_P^2}{C_s D_{eff}} \leq 0.3 \qquad \textbf{(2)}$$

The abovementioned conditions result in a Weisz-Prater number of 0.2, which supports the previous statement that no internal mass transfer limitations are present at these conditions.

4.2.1.2 Temperature Effects

Increasing the temperature should increase the conversion, due to the availability of energy to overcome the energy barrier of the reaction. For the same reason the product distribution can also change because different catalytic pathways could occur, leading to formation of various products. [73,74] Temperatures above 450 °C can however result in irreversible dealumination of the zeolite.[50] ZSM-5 with Si/Al 25 has been used to determine the optimal temperature for BTEX formation, since Slamet et al. have reported it as the best Si/Al ratio for the aromatization of acetone.[49] **Figure 20** shows the product distribution of the reaction of 4-heptanone over ZSM-5 Si/Al 25 at different reaction temperatures after 2.5 h on stream. Multiple trends can be observed in the results. Firstly, temperatures up to 400 °C do not show full conversion. Selectivity towards BTEX increases with temperature, and reaches a maximum of 29 $\%_c$ at 450 °C. Another apparent difference with increasing temperature is the increased formation of short chain olefins. This trend is mentioned in literature for other oxygen containing, biomass derived compounds.[75] The yield denoted as 'other' is the possibility of coke formation and oxygen loss in the form of CO/CO_2. 450 °C is the optimal temperature for the reaction since the BTEX yield is at the highest. Usage of Si/Al 25 was however based on an article with acetone as reactant. The optimum catalyst for the aromatization of 4-heptanone could be a different Si/Al.[49]

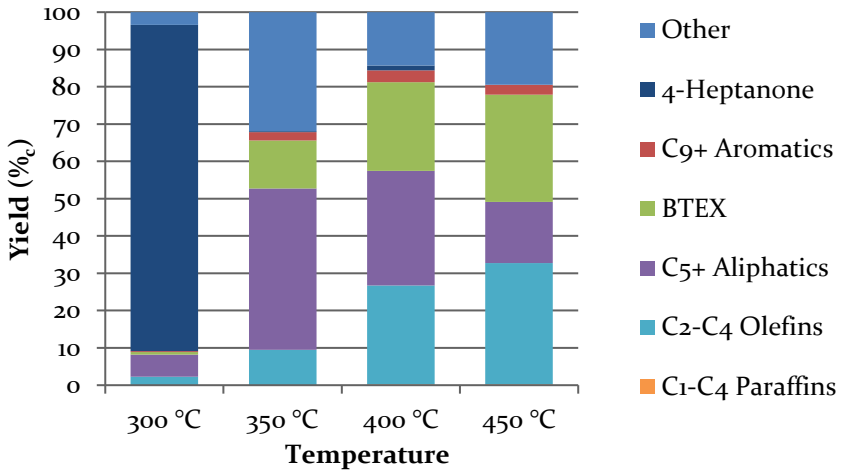

Figure 20 Temperature variation on the reaction of 4-heptanone, 100 mL N2/min, WHSV = 1h-1, ZSM-5 Si/Al 25.

4.2.1.3 *Silicon to Aluminium Ratio Effects*

The Si/Al of a zeolite influences its acid site density and strength.[24,25] This change in acidity can cause a change in the product distribution due to the possibility of cleaving other bonds and following different reaction paths.[76] This can also effect the stability of the catalyst e.g. by the formation of coke.[49,77] The product distributions and activities during the reaction of 4-heptanone over ZSM-5 have been measured at 300 °C for the different catalysts. 300 °C was used to ensure that not all 4-heptanone was converted, and thus the activity could be compared.

Figure 21 shows the conversion of 4-heptanone and the selectivity towards the different products after 1.5 h TOS. The figure indicates that, at a reaction temperature of 300 °C, Si/Al 40 shows the highest activity and selectivity towards BTEX. Si/Al 25 and 11.5 show a slightly lower conversion of 4-heptanone and BTEX yield, while Si/Al 140 barely shows any activity, which is probably due to the low acid site density on the material.

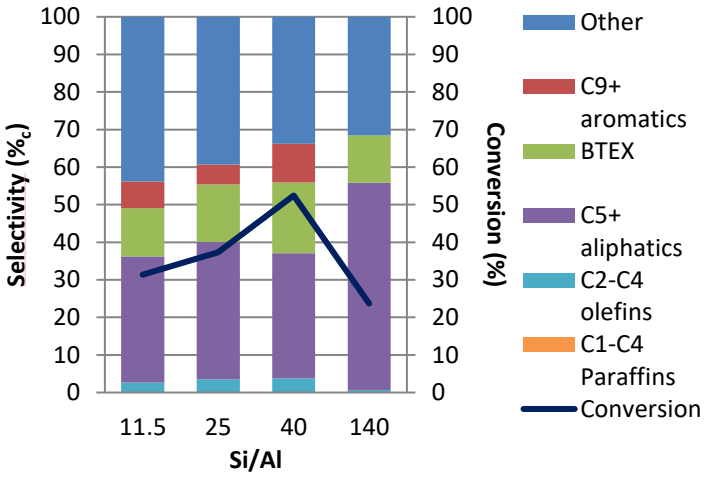

Figure 20 Product distribution after 2.5 h on stream during the reaction of 4-heptanone over ZSM-5 with varying Si/Al at 300 °C.

However, a temperature of 450 °C was found to be the optimum for BTEX formation. Therefore the different Si/Al have also been tested at 450 °C. The results are shown in **Figure 22**. All catalysts show full conversion at this temperature, and at 29 $\%_c$, Si/Al 25 shows the highest yield towards BTEX. The different optimum in Si/Al at different temperatures is due to the amount of available energy. As explained in Chapter 2, the acid strength of a zeolite increases with decreasing aluminium content. For this reason Si/Al 40 has slightly stronger acid sites than Si/Al 25.[24,25] This change in acidity could lower the activation energy needed for the formation of BTEX, which results in Si/Al 40 showing a higher yield to BTEX at lower temperature. However, at higher temperatures this energy is already sufficiently applied by the reactor, resulting that the difference in acid strength between Si/Al 25 and 40 no longer influences the BTEX yield, but instead the amount of acid sites plays the major role between those two catalysts.

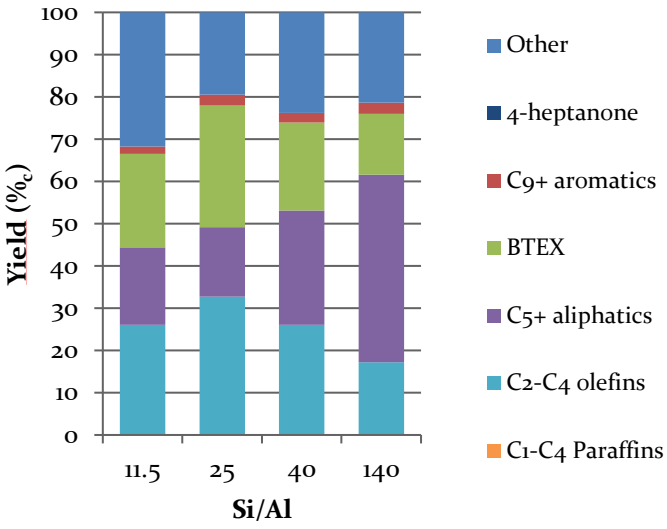

Figure 22 Product distribution after 2.5 h on stream during the reaction of 4-heptanone over ZSM-5 with varying Si/Al at 450 °C.

4.2.1.4 Product Analysis

All experiments were run using on-line GC. Due to the high amount of peaks in the on-line chromatograms, a complete analysis was performed using off-line GC x GC-MS by capturing the products in a liquid nitrogen cold trap. **Figure 23** shows the product mixture of the conversion of 4-heptanone over ZSM-5 Si/Al 25 at 400 °C. The products with low boiling points (C_1-C_5 aliphatics) are expected to have already been evaporated before the measurement. The figure does however show a large product distribution with many different aromatic compounds. The peaks of monoaromatic compounds show the highest intensity in comparison to polyaromatics, which are barely observed in the on-line chromatograms. The following sections will provide attempts on decreasing the product distribution.

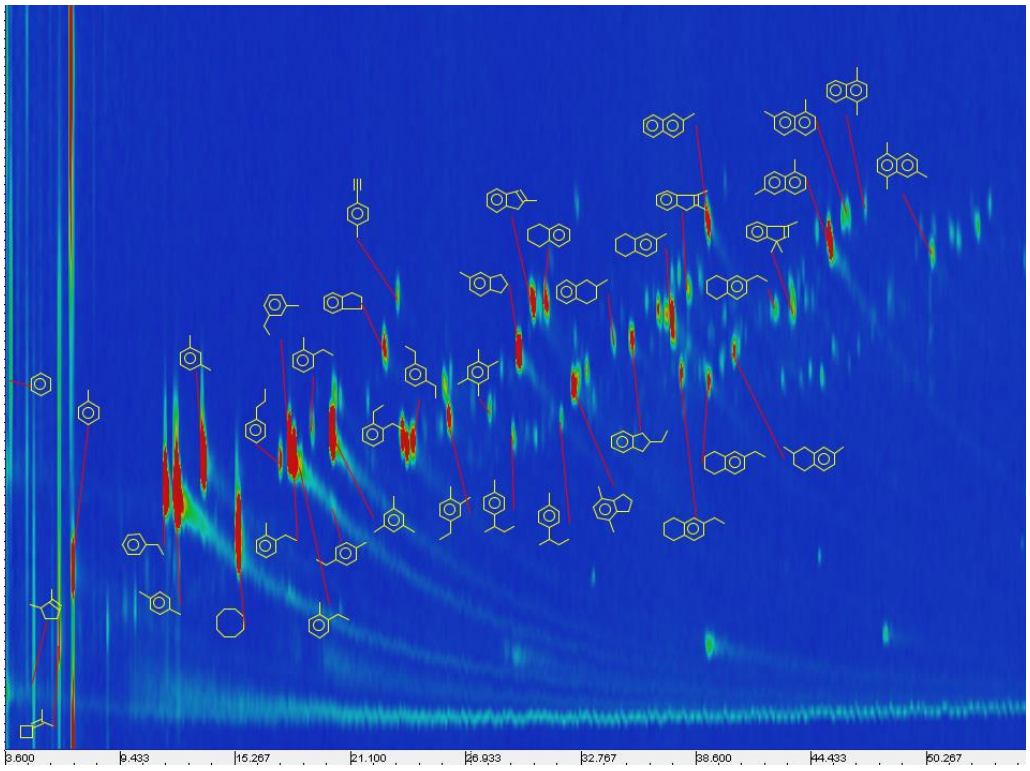

Figure 23 GC x GC-MS spectrum of the product of the reaction of 4-heptanone over ZSM-5 Si/Al 25 at 400 °C with a total TOS of 5.5 h.

4.2.1.5 Ga loading

The obtained products show a wide distribution. Incorporation of gallium should dehydrogenate the cyclohexenes and form more aromatics. As seen in **§4.1.2,** ZSM-5 with 3 wt.% gallium shows both the highest amount of acid sites and the highest percentage active dehydrogenating species, GaO^+. The results of varying the Ga loading on ZSM-5 are shown in **figure 24**. The figure shows that BTEX selectivity reaches an optimum of 66 $\%_c$ with a Ga loading of 3 wt.%. This increase comes with a decrease in formation of (alkylated) cyclohexenes and 'other' compounds. Which is mainly a decrease of short chain paraffins and methylated cyclohexadienes. The product mixture over the 3 wt.% Ga consist mainly of toluene, which is due to dehydrogenation of methylated cyclic C_6 hydrocarbons. This can be seen in **Figure 25**, which shows a gas chromatogram of the reaction after 2.5 hours on stream. Alkylated C_6-rings can be found in between the benzene (retention time = 11 min) and toluene (retention time = 14.7 min). During the reaction of 4-heptanone over 3%Ga-ZSM-5 this area is nearly empty.

According to H_2-TPR, 3 wt.% Ga haz the highest quantity of the active specie (GaO^+), followed by 4.5 wt.% Ga and 1.5 wt.% Ga. The BTEX formation during the reaction follows the same trend with 3 wt.% Ga having the highest BTEX formation, followed by 4.5 and 1.5 wt.%. This is an indication of GaO^+ in fact being the active specie for the aromatization reaction.

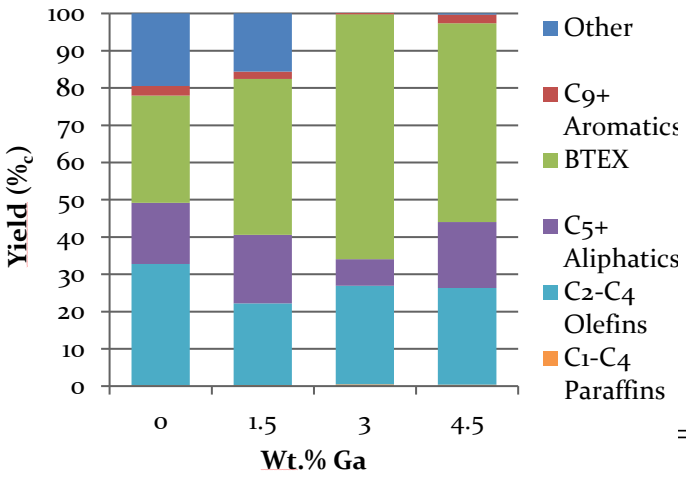

Figure 24 Varying wt.% Ga, 450 °C, WHSV = 1 h^{-1}, Si/Al 25, 100 mL N_2/min

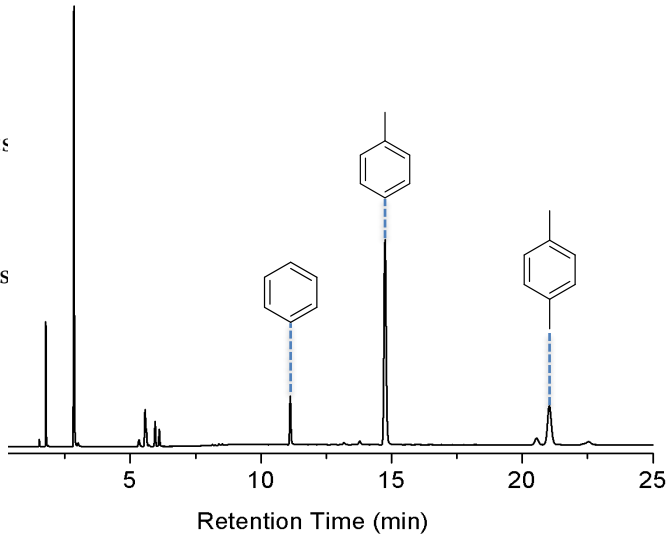

Figure 25 Gas chromatogram of the reaction of 4-heptanone over 3%Ga-ZSM-5 Si/Al at 450 °C after 2.5 h on stream.

4.2.1.6 Pore Modification

In attempt to decrease the product distribution, the pore size of the catalyst was reduced. Reducing the pore openings prevents the formation of C_{9+} aromatics and o/m-xylene due to size constraints.[78] The product distribution of the reactions over the catalysts after 2.5 h on stream at 450 °C are shown in **Figure 26**. The figure shows that the product distribution does not change much for the undoped samples, an increase in alkylated cyclohexenes and a decrease in 'other' products can be observed. This change is probably due to more bulky molecules not being able to leave the cages of the pore-reduced zeolite. These molecules either stay inside the pores as coke, or are dealkylated to form smaller hydrocarbons.

Since ZSM-5 with 3 wt.% Ga showed the optimum BTEX formation, the pore-reduced catalyst was impregnated following the same procedure. The pore-reduced gallium doped samples show a more significant change, mainly a large decrease in BTEX formation from 66 to 43 $\%_C$ upon pore narrowing. This has two possible explanations, either the silylation decreases the amount of acid sites on the zeolite, and thereby decreases the amount of catalytic sites.[52] Or the gallium was not able to enter the pores due to the decreased pore size, and because of this, the distance between the dehydrogenating and acid sites was too large. For this reason, pore modification has not been used in any further experiments.

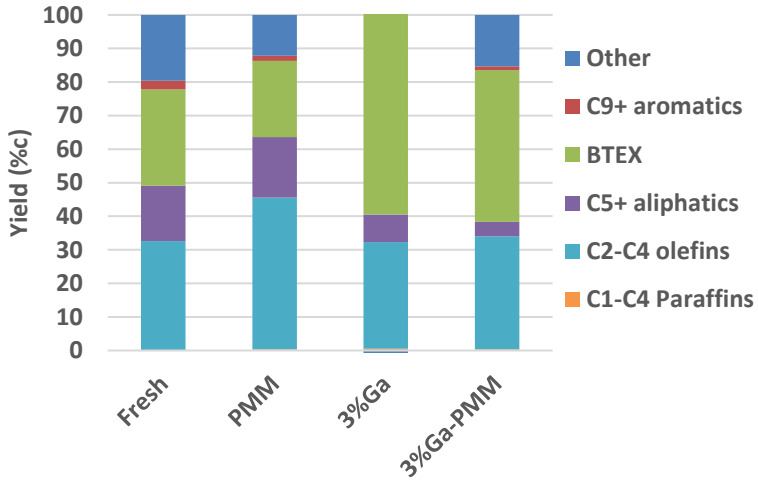

Figure 26 Pore modification and 3%Ga pore reduced at 450 °C, WHSV= 1 h^{-1}, Si/Al 25 and 100 mL N_2/min.

4.2.1.7 Space Velocity

Effect of weight hourly space velocity (WHSV) on the BTEX selectivity was studied Setiadi et al.[48] have reported that 2.18 h^{-1} results in the highest monoaromatic yield out of space velocities of 2.18, 4.74 and 7.13 h^{-1}. Increasing the WHSV reportedly results in a decrease of C_6-C_8 aromatics, while enhancing the selectivity towards C_{9+} aromatics.[48]

The effect of the space velocity on the stability of the Ga-doped catalyst and selectivity toward BTEX have been investigated. The results are shown in **Figure 27**. The different space velocities all deactivate with a linear correlation. The rate of deactivation increases with increasing space velocity. As the catalyst deactivates the BTEX formation is lowered and selectivity to C_{5+} aliphatics rises, indicating deactivation of the gallium species.

A space velocity of 2 h^{-1} shows the lowest initial BTEX yield, this is thought to be due to rapid deactivation. The highest BTEX yield is realised with a space velocity of 1.5 h^{-1}, however, by taking into account the deactivation of the catalysts, 1 h^{-1} is the optimum space velocity for the aromatization of 4-heptanone.

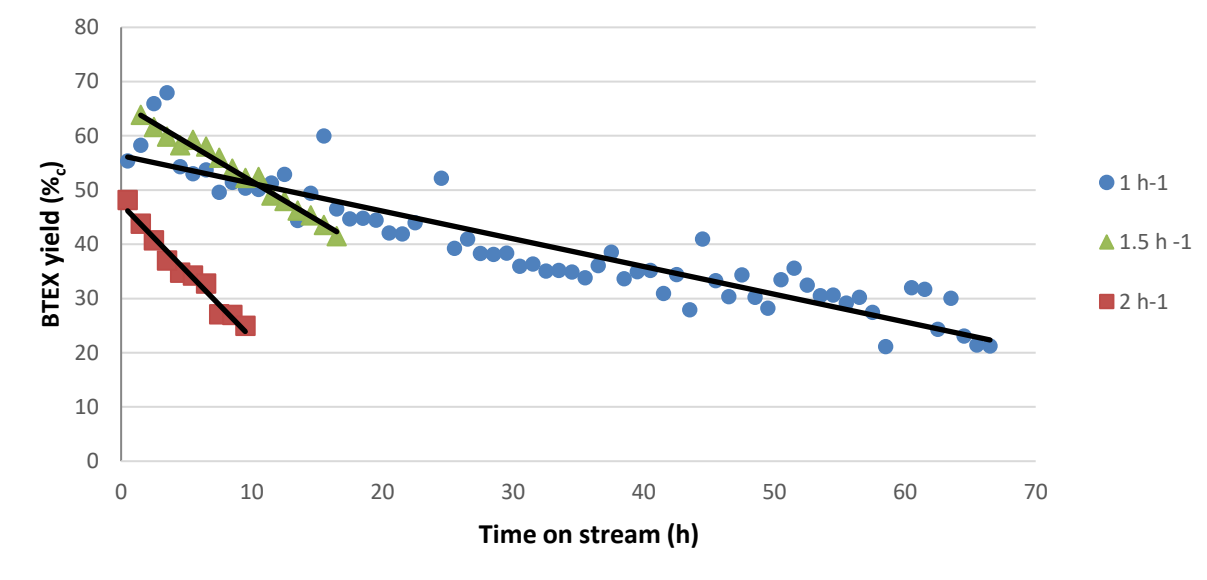

Figure 27 Influence of space velocity on BTEX yield and stability at 450 °C, 100 mL N_2/min and 3%Ga-ZSM-5 Si/Al 25 as a catalyst.

4.2.1.8 Effect of water on stability

According to literature, co-feeding of water over zeolites can suppress the formation of coke, and thereby decrease the rate of deactivation. Stability of 3 wt.%Ga-ZSM-5 was tested with a 40 : 60 vol : vol ratio of 4-heptanone to water and a 4-heptanone space velocity of 1 h^{-1}. **Figure 28** shows the BTEX selectivity of the catalyst over time. The initial BTEX selectivity is 36 $\%_c$ and decreases to 19 $\%_c$ after 50 hours on stream. The rate of deactivation is lower than the samples measure without co-feeding of water. The initial BTEX selectivity is however halved compared to the catalytic test without water. This decrease in initial selectivity is most likely due to water suppressing the dehydrogenating abilities of the gallium species.

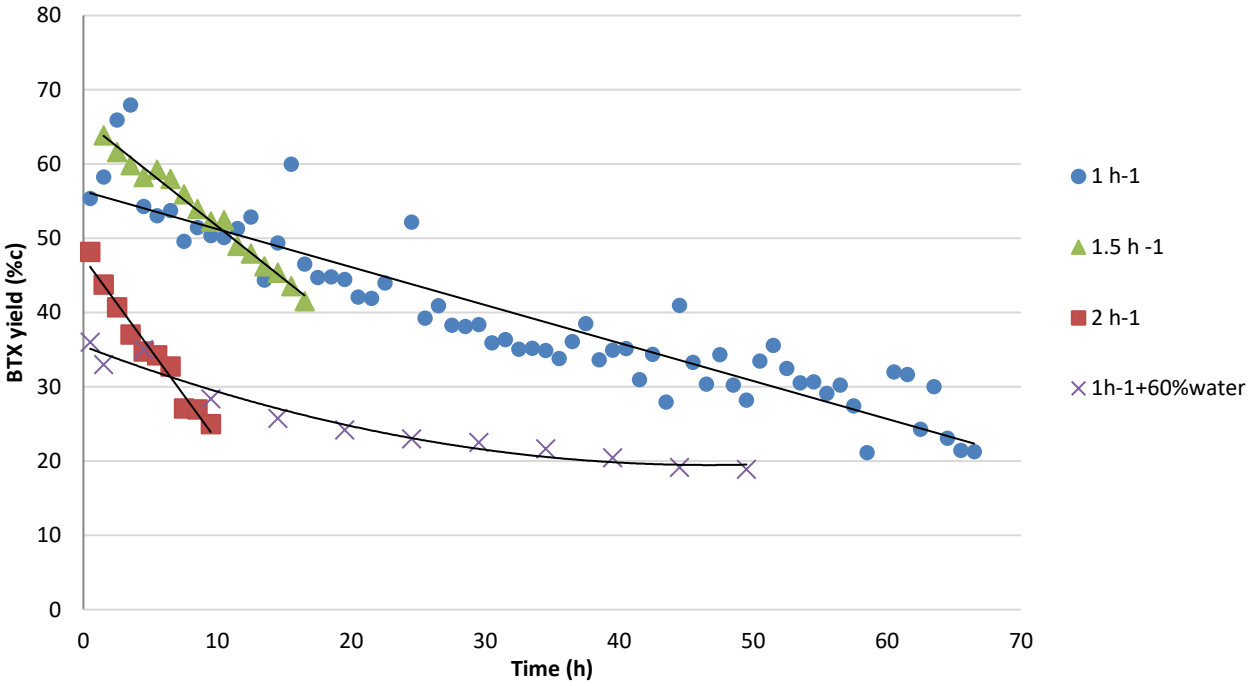

Figure 2821 BTEX yield over time at varying space velocities and the presence of water. Conditions: 100 mL N_2/min, 450 °C, 3%Ga-ZSM-25.

4.3 Conversion of mixed acids

The final objective of the project is the conversion of the reactant mixture provided by fermentation and adsorption, consisting of acetic-, propionic- and butyric acid. This conversion can take place in two ways, either by the direct conversion of the acid mixture over ZSM-5 or by use of a double bed reactor consisting of TiO_2 and ZSM-5.

4.3.1 3%Ga-ZSM-5

Usage of a single catalyst for the conversion of acids to aromatics would increase both the simplicity and cost efficiency of the process. In order to test the viability of this method, volatile fatty acids were fed over 3 wt.%Ga-ZSM-5. A mixture of 1 : 5 : 20 moles of acetic- : propionic- : butyric acid was used as the reaction mixture. The optimal reaction conditions and catalyst for the reaction of 4-heptanone to aromatics were used. The product distribution at different times on stream is shown in **Figure 29**. The figure indicates that VFAs can be converted to BTEX directly by use of gallium impregnated ZSM-5. The selectivity is however lower than the conversion of 4-heptanone to aromatics. With a large portion of the carbon ends up in 'other' molecules, which can be either coke formation or the loss of carbon due to the formation of CO/CO_2 in order to eliminate the oxygen atoms of the VFAs. During this reaction, a mixture of acids is however used instead of just a single component. This mixture of smaller chain molecules could increase the deactivation of the zeolite.

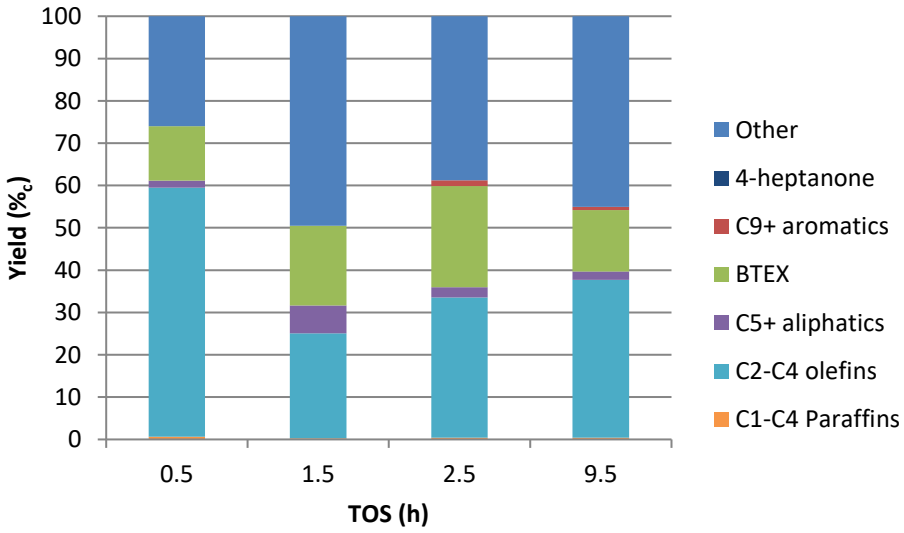

Figure 29 Direct conversion of VFAs over 3%Ga-ZSM-5 Si/Al 25, WHSV = 1 h^{-1}, 100 mL N_2/min, 450 °C.

4.3.2 Dual bed catalysis

Since direct conversion of VFAs to aromatics over Ga-ZSM-5 was unsuccesfull, a dual bed catalyst consisting of TiO_2 and 3 wt.% Ga-ZSM-5 was tested. The first problem encountered during dual bed catalysis is the temperature. The optimal temperature for aromatization is 450 °C, while the ketonization is normally reported to react at lower temperatures.[79] P25 (a physical mixture of 75% anatase and 25% rutile) shows a full conversion of the acid mixture to ketones at 450 °C and a space velocity of 7.2 h^{-1}. However the catalyst deactivates readily, resulting in an increasing amount of carboxylic acids over ZSM-5 over time. **Figure 30** shows the product disribution during the dual bed conversion of mixed VFAs, an initial BTEX selectivity of 37 $\%_c$ is realized but with increasing time on stream the carboxylic acids not converted by titania are converted to short chain olefins by ZSM-5, resulting in a steep decrease of BTEX selectivity over time. After 9.5 h TOS the product distribution resembles the distribution during the direct conversion of VFAs over gallium doped ZSM-5.

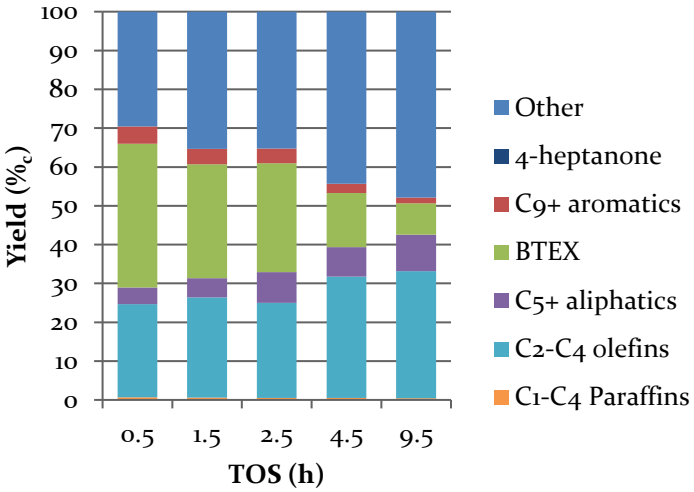

Figure 30 Product distribution upon TOS for dual bed catalysis of P25 and 3%Ga-ZSM-5, 450 °C, 100 mL N_2/min, WHSV = 1 h^{-1}.

5 Conclusion

4-Heptanone was successfully aromatized over ZSM-5. Temperature studies indicated that optimal BTEX selectivity was realized at 450 °C. Silicon to aluminium ratios of 11.5, 25, 40 and 140 were tested for their activity and selectivity in this reaction. A Si/Al of 25 resulted in the highest BTEX yield of 29 $\%_c$. At these reaction conditions a significant amount of the carbon did however end up in short chain olefins and C_{5+} aliphatics.

In attempt to narrow the product distribution during the aromatization of 4-heptanone, the pore size of ZSM-5 was reduced. This modification did not lead to an increase in BTEX selectivity.
A second attempt to narrow the product distribution was the incorporation of gallium in the zeolite.

Gallium was wet-impregnated on ZSM-5 Si/Al 25 with weight percentages of 1.5, 3 and 4.5 % Ga. Analysis by H_2-TPR, TPD-NH_3 and Py-IR indicated that a gallium loading of 3 wt.% inhibits both the highest amount of active phase gallium, GaO^+, and the highest acid site density. Catalytic testing of 4-heptanone to aromatics under the optimum conditions found for the non-doped samples showed that usage of 3 wt.% Ga-ZSM-5 results in a BTEX yield of 66 $\%_c$. This BTEX yield is higher than reported in literature up to this point.

The effect of the weight hourly space velocity on both the selectivity and stability of the catalyst was studied, out of WHSVs of 1, 1.5 and $2h^{-1}$ a space velocity of 1.5 h^{-1} presented the highest initial BTEX selectivity, but had fast deactivation compared to a WHSV of 1 h^{-1}. Combining the BTEX selectivity and stability of the catalyst at different space velocities, a space velocity of 1 h^{-1} was selected to be the optimal.

Further optimization of the process by direct conversion of VFAs over Ga-ZSM-5 resulted in low quantities of BTEX formed with approximately 10-20 $\%_c$ yield. The majority of the carbon content in this reaction ends up in CO, CO_2 and coke.

Dual bed catalysis of TiO_2 and ZSM-5 was not successful due to TiO_2 deactivating readily at the optimal temperature for BTEX formation over ZSM-5.

6 Outlook

In this thesis the main focus has lied with the aromatization of 4-heptanone. In the dual bed conversion of acids, the reactant was however a mixture of acetic-, propionic- and butyric acid. Catalytic tests of the separate ketones could give more insight in the reaction pathway and thereby create the opportunity to further optimise the reaction.

Gallium has only been impregnated on ZSM-5 with a Si/Al of 25. According to literature, gallium is deposited on silicon atoms rather than on aluminium atoms. Decreasing the Si/Al could result in a higher concentration of the active species for the dehydrogenation step for the reaction. Therefore impregnating ZSM-5 Si/Al of 11.5 with gallium could result in a higher BTEX selectivity.

At the same time, after gallium impregnation the dispersant was removed by rotation evaporation. This evaporating of the solvent can have caused the formation of “hot spots” of gallium on the surface of the zeolite. Other drying methods such as freeze-drying could therefore result in a better distribution of the gallium species, and thus lower percentages of gallium ending up in bulk Ga_2O_3 particles.

During the conversion of VFAs over a dual catalytic bed, both of the catalysts were placed in a single oven with a single temperature. By using an oven with either a temperature gradient or two separate ovens, both catalysts can react under their perfect conditions, optimizing the results of the reaction.

In this thesis, no research has been performed on the cause of deactivation of the catalyst. Analysing the spent catalyst by TGA-MS could indicate the extend of coke formation on the catalyst. Whereas post-reaction H_2-TPR could indicate the deactivation of gallium by reduction. If the catalyst is deactivated by coke formation, it could be regenerated by increasing the temperature in an oxygen rich environment. While if the catalyst deactivated by reduction of the gallium species, oxidation of Ga^+ to GaO^+ by NO could recover the activity and selectivity of the catalyst after a significant time on stream.[30]

Acknowledgements

During my time at ICC over the past year and a bit I have received a lot of help from different people, I would like to take a moment to express my gratitude. First and foremost, I would like to thank my daily supervisor, Egor Fufachev for his help during the project. Both during and outside of office-hours he would give me feedback on my analysis, poster, presentations and on my thesis.

I would like to thank Pieter Bruijnincx for giving me the opportunity to do my masters research at this group, for the helpful discussions and commentary on my presentations. But also for making sure I did not wander off too far in the sea of endless possibilities to pursue, or in short: 'It's better to do one thing properly than to do many things partly'. Also I would like to thank Gareth for being my second examiner and the feedback during my go/no-go and poster presentation.

Furthermore I would like to thank Lennart for all his help with GC analysis and the mechanics of the set-up. Nynke, Wouter and Mark for spending their time to help me measure my different samples on (S)TEM, Ana and Marjolein and Paul for their help with using and analysing pyridine-IR, Beatriz for her help on the analysis of Ga-impregnation of zeolites and Ramon for being my supervisor when Egor was absent.

Lastly, I would like to thank ICC, for its fun borrels, lunchbreaks, coffee breaks, Christmas dinners, barbeques and the labuitje. However, mainly for making me feel welcome, and enjoy the time I spent here.

Bibliography

(1) Park, Y.-K.; Lee, C. W.; Kang, N. Y.; Choi, W. C.; Choi, S.; Oh, S. H.; Park, D. S. Catalytic Cracking of Lower-Valued Hydrocarbons for Producing Light Olefins. *Catal. Surv. from Asia* **2010**, *14* (2), 75–84.

(2) Alonso, D. M.; Bond, J. Q.; Dumesic, J. A. Catalytic Conversion of Biomass to Biofuels. *Green Chem.* **2010**, *12* (9), 1493.

(3) Naik, S. N.; Goud, V. V.; Rout, P. K.; Dalai, A. K. Production of First and Second Generation Biofuels: A Comprehensive Review. *Renew. Sustain. Energy Rev.* **2010**, *14* (2), 578–597.

(4) Jiang, Y.; Marang, L.; Tamis, J.; van Loosdrecht, M. C. M.; Dijkman, H.; Kleerebezem, R. Waste to Resource: Converting Paper Mill Wastewater to Bioplastic. *Water Res.* **2012**, *46* (17), 5517–5530.

(5) Dwidar, M.; Park, J.-Y.; Mitchell, R. J.; Sang, B.-I. The Future of Butyric Acid in Industry. *Sci. World J.* **2012**, *2012*, 1–10.

(6) López-Garzón, C. S.; Straathof, A. J. J. Recovery of Carboxylic Acids Produced by Fermentation. *Biotechnol. Adv.* **2014**, *32* (5), 873–904.

(7) Xu, Z.; Shi, Z.; Jiang, L. Acetic and Propionic Acids. In *Comprehensive Biotechnology*; Elsevier, 2011; Vol. 3, pp 189–199.

(8) Liu, L.; Zhu, Y.; Li, J.; Wang, M.; Lee, P.; Du, G.; Chen, J. Microbial Production of Propionic Acid from Propionibacteria: Current State, Challenges and Perspectives. *Crit. Rev. Biotechnol.* **2012**, *32* (4), 374–381.

(9) Reyhanitash, E.; Zaalberg, B.; Kersten, S. R. A.; Schuur, B. Extraction of Volatile Fatty Acids from Fermented Wastewater. *Sep. Purif. Technol.* **2016**, *161*, 61–68.

(10) Reyhanitash, E.; Kersten, S. R. A.; Schuur, B. Recovery of Volatile Fatty Acids from Fermented Wastewater by Adsorption. *ACS Sustain. Chem. Eng.* **2017**, *5* (10), 9176–9184.

(11) Pham, T. N.; Sooknoi, T.; Crossley, S. P.; Resasco, D. E. Ketonization of Carboxylic Acids: Mechanisms, Catalysts, and Implications for Biomass Conversion. *ACS Catal.* **2013**, *3* (11), 2456–2473.

(12) Basagiannis, A. C.; Verykios, X. E. Reforming Reactions of Acetic Acid on Nickel Catalysts over a Wide Temperature Range. *Appl. Catal. A Gen.* **2006**, *308*, 182–193.

(13) Tosoni, S.; Pacchioni, G. Acetic Acid Ketonization on Tetragonal Zirconia: Role of Surface Reduction. *J. Catal.* **2016**, *344*, 465–473.

(14) Murkute, A. D.; Jackson, J. E.; Miller, D. J. Supported Mesoporous Solid Base Catalysts for Condensation of Carboxylic Acids. *J. Catal.* **2011**, *278* (2), 189–199.

(15) Zukauskas, V. Aromatics. *Encycl. Hydrocarb.* **2005**, *2*, 592.

(16) Bender, M. Global Aromatics Supply - Today and Tomorrow. *DGMK Tagungsbericht* **2013**, *2013* (2), 59–65.

(17) Caeiro, G.; Carvalho, R. H.; Wang, X.; Lemos, M. A. N. D. A.; Lemos, F.; Guisnet, M.; Ramôa

Ribeiro, F. Activation of C2-C4alkanes over Acid and Bifunctional Zeolite Catalysts. *J. Mol. Catal. A Chem.* **2006**, *255* (1–2), 131–158.

(18) Cundy, C. S.; Cox, P. A. The Hydrothermal Synthesis of Zeolites: History and Development from the Earliest Days to the Present Time. *Chem. Rev.* **2003**, *103* (3), 663–702.

(19) Derouane, E. G. On the Physical State of Molecules in Microporous Solids. *Microporous Mesoporous Mater.* **2007**, *104* (1–3), 46–51.

(20) Sang, S.; Chang, F.; Liu, Z.; He, C.; He, Y.; Xu, L. Difference of ZSM-5 Zeolites Synthesized with Various Templates. *Catal. Today* **2004**, *93–95*, 729–734.

(21) Deka, R. C. Acidity in Zeolites and Their Characterization by Different Spectroscopic Methods. *Indian J. Chem. Technol.* **1998**, *5* (3), 109–123.

(22) Shirazi, L.; Jamshidi, E.; Ghasemi, M. R. The Effect of Si/Al Ratio of ZSM-5 Zeolite on Its Morphology, Acidity and Crystal Size. *Cryst. Res. Technol.* **2008**, *43* (12), 1300–1306.

(23) Duminda, A.; Sandun, D. Methods and Applications of Deoxygenation for the Conversion of Biomass to Petrochemical Products. In *Biomass Now - Cultivation and Utilization*; InTech, 2013; pp 273–298.

(24) Szabo, S.; Menezo, J. C.; Montassier, C.; Naja, J.; Del, G.; Dominguez, J. M.; Boitiaw, J. P.; Chaumette, P.; Leporq, S.; Barbier, J.; et al. *Handbook of Heterogeneous Catalysis*; Ertl, G., Knzinger, H., Weitkamp, J., Eds.; Wiley-VCH Verlag GmbH: Weinheim, Germany, 1997.

(25) Rice, M. J.; Chakraborty, A. K.; Bell, A. T. Al Next Nearest Neighbor, Ring Occupation, and Proximity Statistics in ZSM-5. *J. Catal.* **1999**, *186* (1), 222–227.

(26) Bartholomew, C. H. Mechanisms of Catalyst Deactivation. *Appl. Catal. A Gen.* **2001**, *212* (1–2), 17–60.

(27) Lukyanov, D. B.; Gnep, N. S.; Guisnet, M. R. Kinetic Modeling of Ethene and Propene Aromatization over HZSM-5 and GaHZSM-5. *Ind. Eng. Chem. Res.* **1994**, *33* (2), 223–234.

(28) Rane, N.; Kersbulck, M.; van Santen, R. A.; Hensen, E. J. M. Cracking of N-Heptane over Brønsted Acid Sites and Lewis Acid Ga Sites in ZSM-5 Zeolite. *Microporous Mesoporous Mater.* **2008**, *110* (2–3), 279–291.

(29) Gnep, N. S.; Doyemet, J. Y.; Seco, A. M.; Ribeiro, F. R.; Guisnet, M. Conversion of Light Alkanes to Aromatic Hydrocarbons. *Appl. Catal.* **1988**, *43* (1), 155–166.

(30) Rane, N.; Overweg, A.; Kazansky, V.; Vansanten, R.; Hensen, E. Characterization and Reactivity of Ga+ and GaO+ Cations in Zeolite ZSM-5. *J. Catal.* **2006**, *239* (2), 478–485.

(31) Tshabalala, T. E.; Scurrell, M. S. Aromatization of N-Hexane over Ga, Mo and Zn Modified H-ZSM-5 Zeolite Catalysts. *Catal. Commun.* **2015**, *72*, 49–52.

(32) Shibata, M.; Kitagawa, H.; Sendoda, Y.; Ono, Y. Transformation of Propene into Aromatic Hydrocarbons over ZSM-5 Zeolites. In *Studies in Surface Science and Catalysis*; 1986; Vol. 28, pp 717–724.

(33) Asaftei, I. V.; Bilba, N.; Sandu, I. Synthesis, Characterization and Catalytic Activity of Gallium-Modified ZSM-5 (MFI) Zeolites in N-Heptane Aromatization. *Rev. Chim.* **2013**, *64* (5), 509–515.

(34) Chang, C. D.; Silvestri, A. J. The Conversion of Methanol and Other O-Compounds to

Hydrocarbons over Zeolit Catalysts. *J. Catal.* **1977**, *259*, 249–259.

(35) Olsbye, U.; Svelle, S.; Bjørgen, M.; Beato, P.; Janssens, T. V. W.; Joensen, F.; Bordiga, S.; Lillerud, K. P. Conversion of Methanol to Hydrocarbons: How Zeolite Cavity and Pore Size Controls Product Selectivity. *Angew. Chemie Int. Ed.* **2012**, *51* (24), 5810–5831.

(36) Bozzano, G.; Manenti, F. Efficient Methanol Synthesis: Perspectives, Technologies and Optimization Strategies. *Prog. Energy Combust. Sci.* **2016**, *56*, 71–105.

(37) Wan, Z.; Wu, W.; Li, G.; Wang, C.; Yang, H.; Zhang, D. Effect of SiO2/Al2O3 Ratio on the Performance of Nanocrystal ZSM-5 Zeolite Catalysts in Methanol to Gasoline Conversion. *Appl. Catal. A Gen.* **2016**, *523*, 312–320.

(38) Stöcker, M. Methanol-to-Hydrocarbons: Catalytic Materials and Their Behavior. *Microporous Mesoporous Mater.* **1999**, *29* (1–2), 3–48.

(39) Wan, H.; Chitta, P. Catalytic Conversion of Propane to BTX over Ga, Zn, Mo, and Re Impregnated ZSM-5 Catalysts. *J. Anal. Appl. Pyrolysis* **2016**, *121*, 369–375.

(40) Martinez-Espin, J. S.; Mortén, M.; Janssens, T. V. W.; Svelle, S.; Beato, P.; Olsbye, U. New Insights into Catalyst Deactivation and Product Distribution of Zeolites in the Methanol-to-Hydrocarbons (MTH) Reaction with Methanol and Dimethyl Ether Feeds. *Catal. Sci. Technol.* **2017**, *7* (13), 2700–2716.

(41) Müller, S.; Liu, Y.; Vishnuvarthan, M.; Sun, X.; van Veen, A. C.; Haller, G. L.; Sanchez-Sanchez, M.; Lercher, J. A. *Coke Formation and Deactivation Pathways on H-ZSM-5 in the Conversion of Methanol to Olefins*; 2015; Vol. 325, pp 48–59.

(42) Czernik, S.; Bridgwater, A. V. Overview of Applications of Biomass Fast Pyrolysis Oil. *Energy & Fuels* **2004**, *18* (2), 590–598.

(43) Mohan, D.; Pittman, C. U.; Steele, P. H. Pyrolysis of Wood/Biomass for Bio-Oil: A Critical Review. *Energy & Fuels* **2006**, *20* (3), 848–889.

(44) Zhu, X.; Lobban, L. L.; Mallinson, R. G.; Resasco, D. E. Tailoring the Mesopore Structure of HZSM-5 to Control Product Distribution in the Conversion of Propanal. *J. Catal.* **2010**, *271* (1), 88–98.

(45) Hoang, T. Q.; Zhu, X.; Sooknoi, T.; Resasco, D. E.; Mallinson, R. G. A Comparison of the Reactivities of Propanal and Propylene on HZSM-5. *J. Catal.* **2010**, *271* (2), 201–208.

(46) Ali, S. A.; Aitani, A. M.; Čejka, J.; Al-Khattaf, S. S. Selective Production of Xylenes from Alkyl-Aromatics and Heavy Reformates over Dual-Zeolite Catalyst. *Catal. Today* **2015**, *243* (C), 118–127.

(47) Nedomová, K.; Beran, S.; Jiru, P. Reactions of Aliphatic Ketones on Zeolites. *React. Kinet. Cat. Lett.* **1986**, *32* (2), 353–357.

(48) Setiadi, S.; Kojima, T.; Tsutsui, T. Conversion of Acetone to Aromatic Chemicals with HZSM-5. **2003**, *932*, 926–932.

(49) Slamet, S.; Mohammad, N. Catalytic Conversion of Acetone to Monoaromatic Chemicals Using HZSM-5. *Int. J. Eng. Technol* **2011**, *11* (2), 72–79.

(50) Gayubo, A. G.; Aguayo, A. T.; Atutxa, A.; Aguado, R.; Olazar, M.; Bilbao, J. Transformation of Oxygenate Components of Biomass Pyrolysis Oil on a HZSM-5 Zeolite. II. Aldehydes, Ketones, and Acids. *Ind. Eng. Chem. Res.* **2004**, *43* (11), 2619–2626.

(51) Fuhse, J.; Bandermann, F. Conversion of Organic Oxygen Compounds and Their Mixtures on H-ZSM-5. *Chem. Eng. Technol. - CET* **1987**, *10* (1), 323–329.

(52) Zheng, S.; Heydenrych, H. R.; Jentys, A.; Lercher, J. A. Influence of Surface Modification on the Acid Site Distribution of HZSM-5 †. *J. Phys. Chem. B* **2002**, *106* (37), 9552–9558.

(53) International Zeolite Association. Structure database http://www.iza-structure.org/databases/ (accessed Jan 6, 2018).

(54) Vankoningsveld, H.; Jansen, J.; Vanbekkum, H. The Monoclinic Framework Structure of Zeolite H-ZSM-5. Comparison with the Orthorhombic Framework of as-Synthesized ZSM-5. *Zeolites* **1990**, *10* (4), 235–242.

(55) Groen, J. C.; Peffer, L. A. A.; Pérez-Ramírez, J. Pore Size Determination in Modified Micro- and Mesoporous Materials. Pitfalls and Limitations in Gas Adsorption Data Analysis. *Microporous Mesoporous Mater.* **2003**, *60* (1–3), 1–17.

(56) Thommes, M.; Kaneko, K.; Neimark, A. V.; Olivier, J. P.; Rodriguez-Reinoso, F.; Rouquerol, J.; Sing, K. S. W. Physisorption of Gases, with Special Reference to the Evaluation of Surface Area and Pore Size Distribution (IUPAC Technical Report). *Pure Appl. Chem.* **2015**, *87* (9–10), 1051–1069.

(57) Groen, J. C.; Pérez-Ramírez, J.; Peffer, L. a. a. Formation of Uniform Mesopores in ZSM-5 Zeolite upon Alkaline Post-Treatment? *Chem. Lett.* **2002**, *31* (1), 94–95.

(58) Bjørgen, M.; Joensen, F.; Spangsberg Holm, M.; Olsbye, U.; Lillerud, K.-P.; Svelle, S. Methanol to Gasoline over Zeolite H-ZSM-5: Improved Catalyst Performance by Treatment with NaOH. *Appl. Catal. A Gen.* **2008**, *345* (1), 43–50.

(59) Rodríguez-González, L.; Hermes, F.; Bertmer, M.; Rodríguez-Castellón, E.; Jiménez-López, A.; Simon, U. The Acid Properties of H-ZSM-5 as Studied by NH3-TPD and 27Al-MAS-NMR Spectroscopy. *Appl. Catal. A Gen.* **2007**, *328* (2), 174–182.

(60) Lezcano-Gonzalez, I.; Deka, U.; Arstad, B.; Van Yperen-De Deyne, A.; Hemelsoet, K.; Waroquier, M.; Van Speybroeck, V.; Weckhuysen, B. M.; Beale, A. M. Determining the Storage, Availability and Reactivity of NH 3 within Cu-Chabazite-Based Ammonia Selective Catalytic Reduction Systems. *Phys. Chem. Chem. Phys.* **2014**, *16* (4), 1639–1650.

(61) Nowak, I.; Quartararo, J.; Derouane, E. G.; Védrine, J. C. Effect of H2-O2pre-Treatments on the State of Gallium in Ga/H-ZSM-5 Propane Aromatisation Catalysts. *Appl. Catal. A Gen.* **2003**, *251* (1), 107–120.

(62) Xiao, H.; Zhang, J.; Wang, X.; Zhang, Q.; Xie, H.; Han, Y.; Tan, Y. A Highly Efficient Ga/ZSM-5 Catalyst Prepared by Formic Acid Impregnation and in Situ Treatment for Propane Aromatization. *Catal. Sci. Technol.* **2015**, *5* (8), 4081–4090.

(63) Busch, O. M.; Brijoux, W.; Thomson, S.; Schüth, F. Spatially Resolving Infrared Spectroscopy for Parallelized Characterization of Acid Sites of Catalysts via Pyridine Sorption: Possibilities and Limitations. *J. Catal.* **2004**, *222* (1), 174–179.

(64) Barzetti, T.; Selli, E.; Moscotti, D.; Forni, L. Pyridine and Ammonia as Probes for FTIR Analysis of Solid Acid Catalysts. *J. Chem. Soc. Faraday Trans.* **1996**, *92* (8), 1401.

(65) CAEIRO, G.; LOPES, J.; MAGNOUX, P.; AYRAULT, P.; RAMOARIBEIRO, F. A FT-IR Study of Deactivation Phenomena during Methylcyclohexane Transformation on H-USY Zeolites:

Nitrogen Poisoning, Coke Formation, and Acidity–activity Correlations. *J. Catal.* **2007**, *249* (2), 234–243.

(66) Kondo, J. N.; Nishitani, R.; Yoda, E.; Yokoi, T.; Tatsumi, T.; Domen, K. A Comparative IR Characterization of Acidic Sites on HY Zeolite by Pyridine and CO Probes with Silica–alumina and γ-Alumina References. *Phys. Chem. Chem. Phys.* **2010**, *12* (37), 11576.

(67) Travert, A.; Vimont, A.; Sahibed-Dine, A.; Daturi, M.; Lavalley, J.-C. Use of Pyridine CH(D) Vibrations for the Study of Lewis Acidity of Metal Oxides. *Appl. Catal. A Gen.* **2006**, *307* (1), 98–107.

(68) Hernández-Giménez, A. M.; Ruiz-Martínez, J.; Puértolas, B.; Pérez-Ramírez, J.; Bruijnincx, P. C. A.; Weckhuysen, B. M. Operando Spectroscopy of the Gas-Phase Aldol Condensation of Propanal over Solid Base Catalysts. *Top. Catal.* **2017**, *60* (19–20), 1522–1536.

(69) Emeis, C. A. Determination of Integrated Molar Extinction Coefficients for Infrared Absorption Bands of Pyridine Adsorbed on Solid Acid Catalysts. *J. Catal.* **1993**, *141* (2), 347–354.

(70) Scott Fogler, H. *Elements of Chemical Reaction Engineering*, 4th ed.; 2005; Vol. 42.

(71) Pham, T. N.; Shi, D.; Resasco, D. E. Kinetics and Mechanism of Ketonization of Acetic Acid on Ru/TiO2 Catalyst. *Top. Catal.* **2014**, *57* (6–9), 706–714.

(72) Weisz, P. B.; Prater, C. D. Interpretation of Measurements in Experimental Catalysis. In *Advances in Catalysis*; 1954; Vol. 6, pp 143–196.

(73) Bayat, A.; Sadrameli, S. M. Production of Renewable Aromatic Hydrocarbons via Conversion of Canola Oil Methyl Ester (CME) over Zinc Promoted HZSM-5 Catalysts. *Renew. Energy* **2017**, *106*, 62–67.

(74) Bayat, A.; Sadrameli, S. M.; Towfighi, J. Production of Green Aromatics via Catalytic Cracking of Canola Oil Methyl Ester (CME) Using HZSM-5 Catalyst with Different Si/Al Ratios. *Fuel* **2016**, *180*, 244–255.

(75) Williams, P. T.; Horne, P. A. Characterisation of Oils From the Fluidised Bed Pyrolysis of Biomass With Zeolite Catalyst Upgrading. *Biomass and Bioenergy* **1995**, *7*, 223–236.

(76) Ben, H.; Ragauskas, A. J. Influence of Si/Al Ratio of ZSM-5 Zeolite on the Properties of Lignin Pyrolysis Products. *ACS Sustain. Chem. Eng.* **2013**, *1* (3), 316–324.

(77) Nasikin, M.; Tsutsui, T.; Kojima, T. Change in Catalytic Activity on Acetone Conversion to Aromatic Chemicals Using H-ZSM-5. **2008**, *2008* (October), 464–468.

(78) Cheng, Y.-T.; Wang, Z.; Gilbert, C. J.; Fan, W.; Huber, G. W. Production of P -Xylene from Biomass by Catalytic Fast Pyrolysis Using ZSM-5 Catalysts with Reduced Pore Openings. *Angew. Chemie Int. Ed.* **2012**, *51* (44), 11097–11100.

(79) Ignatchenko, A. V.; DeRaddo, J. S.; Marino, V. J.; Mercado, A. Cross-Selectivity in the Catalytic Ketonization of Carboxylic Acids. *Appl. Catal. A Gen.* **2015**, *498*, 10–24.

Appendix

A Ar-physisorption

A 1 BET-analysis

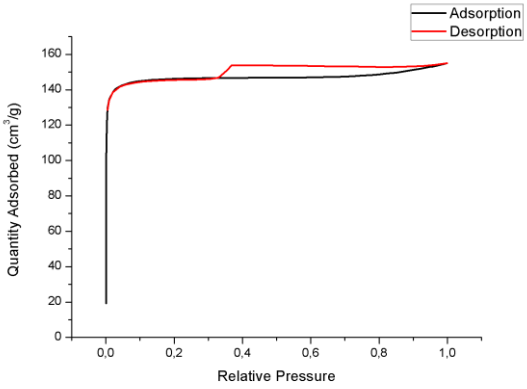

A 1 BET-analysis of ZSM-5 Si/Al 11.5.

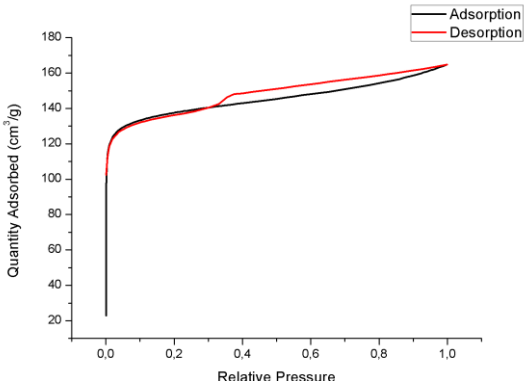

A 2 BET-analysis of ZSM-5 Si/Al 25.

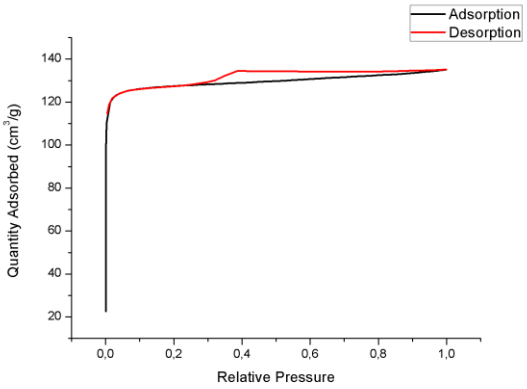

A 3 BET-analysis of ZSM-5 Si/Al 40.

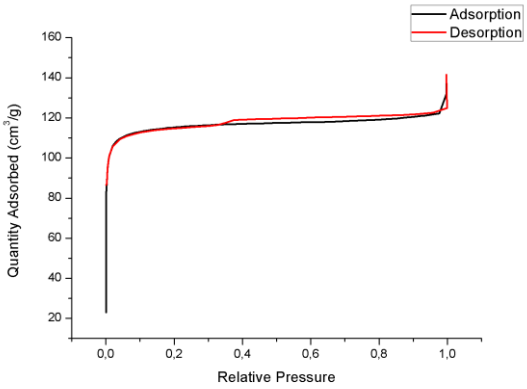

A 4 BET-analysis of ZSM-5 Si/Al 140.

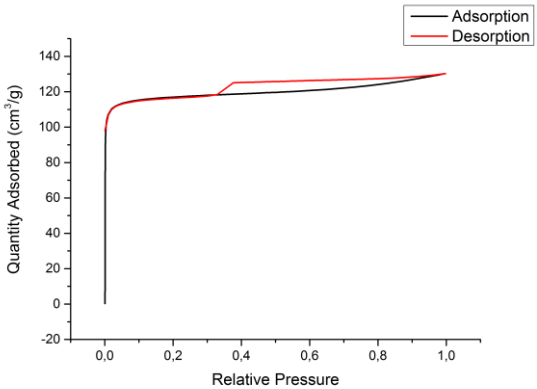

A 5 BET-analysis of 1.5 wt.% Ga-ZSM-5 Si/Al 25.

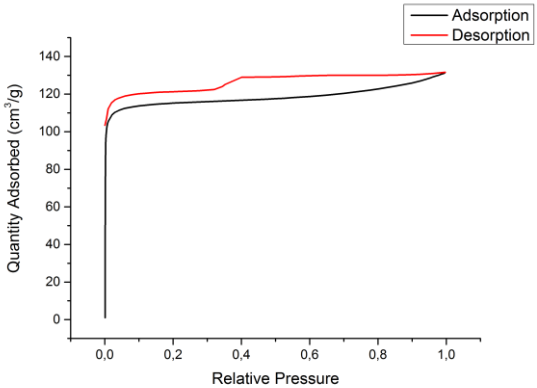

A 6 BET-analysis of 3 wt.% Ga-ZSM-5 Si/Al 25.

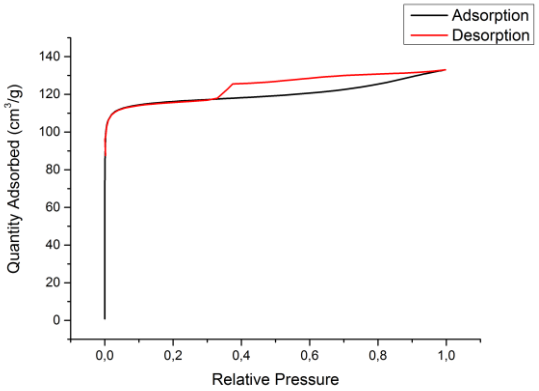

A 7 BET-analysis of 4.5 wt.% Ga-ZSM-5 Si/Al 25.

A 2 BJH-analysis

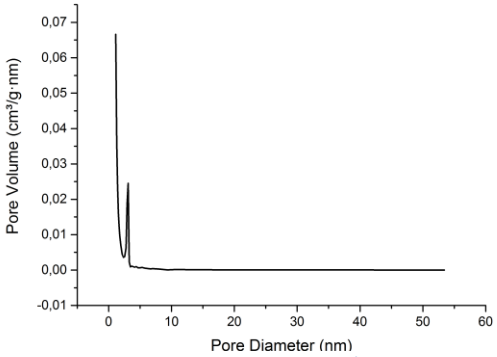

A 8 BJH-analysis of ZSM-5 Si/Al 11.5.

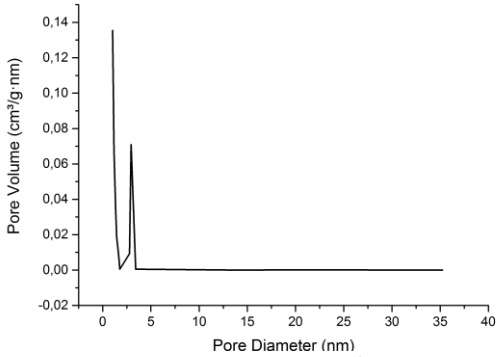

A 9 BJH-analysis of ZSM-5 Si/Al 25.

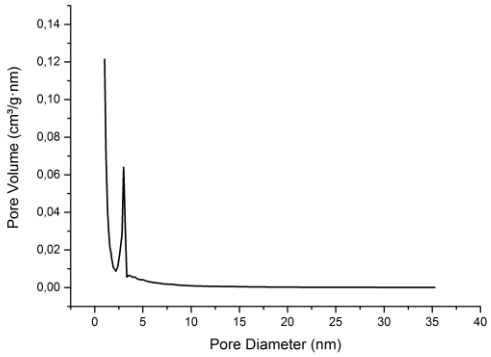

A 10 BJH-analysis of ZSM-5 Si/Al 40.

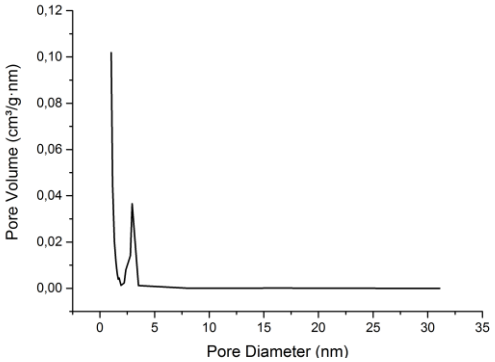

A 11 BJH-analysis of ZSM-5 Si/Al 140.

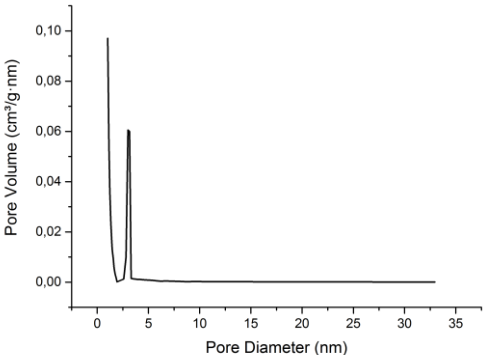

A 12 BJH-analysis of 1.5 wt.% Ga-ZSM-5 Si/Al 25.

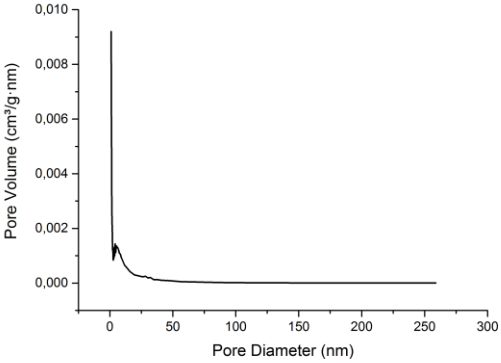

A 13 BJH-analysis of 3 wt.% Ga-ZSM-5 Si/Al 25.

B TPD-NH_3

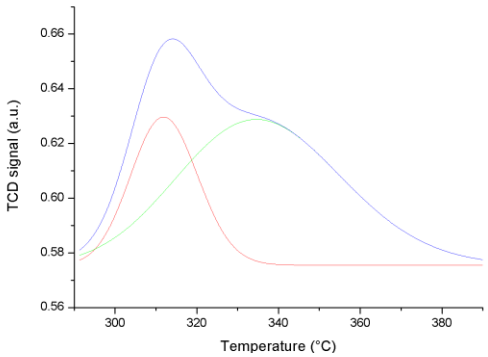

B 1 TPD-NH_3 of ZSM-5 Si/Al 11.5. The blue profile indicates the actual measurement.

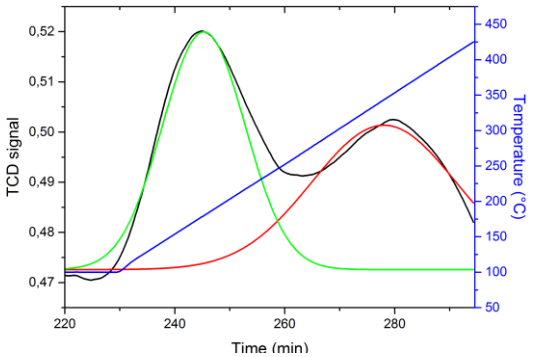

B 2 TPD-NH_3 of ZSM-5 Si/Al 25. The black profile indicates the actual measurement.

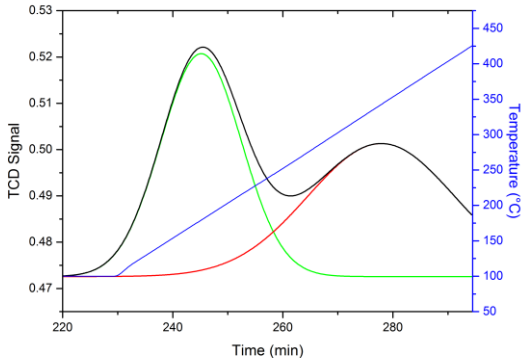

B 3 TPD-NH_3 of ZSM-5 Si/Al 40. The black profile indicates the actual measurement.

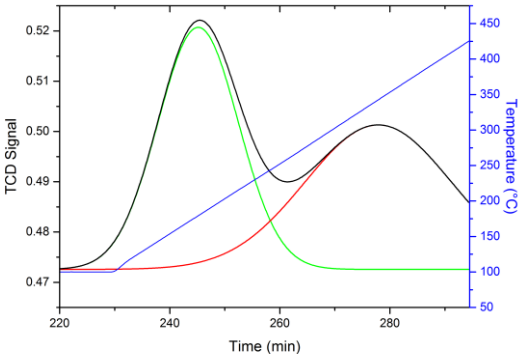

B 4 TPD-NH_3 of ZSM-5 Si/Al 140. The black profile indicates the actual measurement.

C H_2-TPR

.

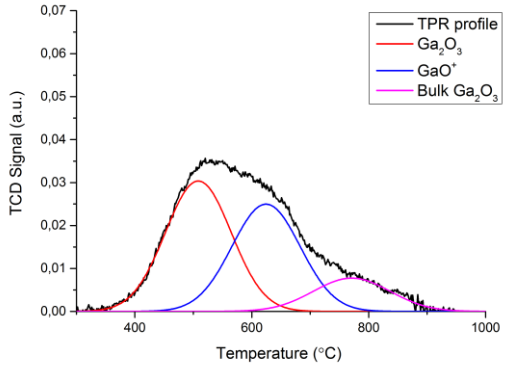

C 1 Deconvoluted reduction profile of 1.5%Ga-ZSM-5 Si/Al 25.

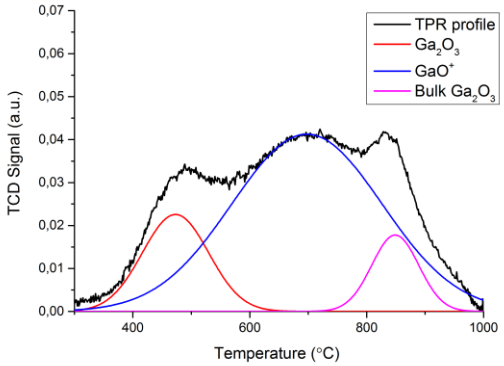

C 2 Deconvoluted reduction profile of 3%Ga-ZSM-5 Si/Al 25.

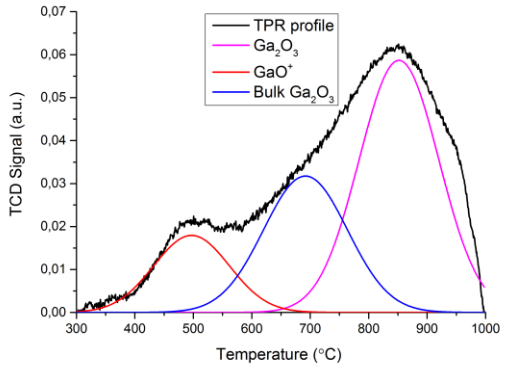

C 3 Deconvoluted reduction profile of 4.5%Ga-ZSM-5 Si/Al 25.

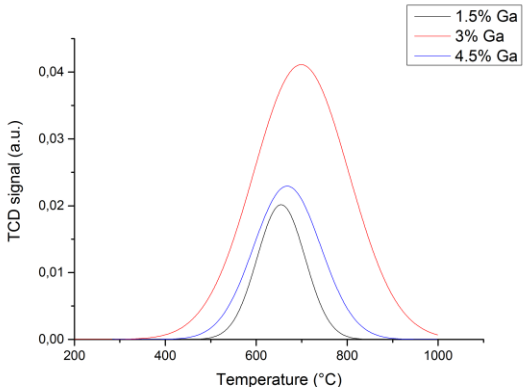

C 4 comparison of GaO^+ reduction peak in different zeolite samples.

D Py-IR

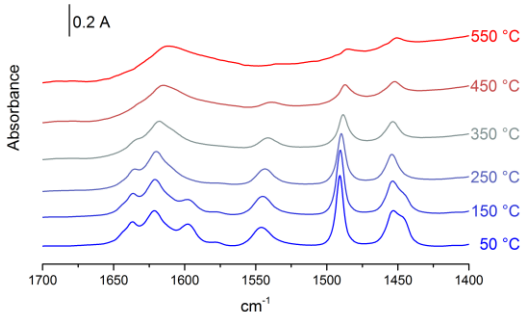

D 1 IR-spectra on Pyridine desorption of ZSM-5 Si/Al 25

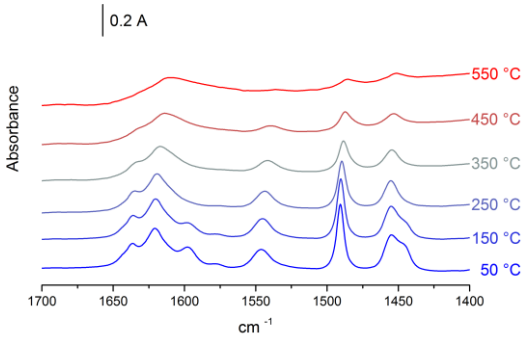

D 2 IR-spectra on Pyridine desorption of 1.5%Ga ZSM-5 Si/Al 25

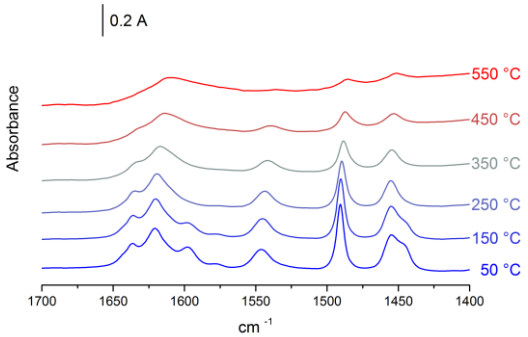

D 3 IR-spectra on Pyridine desorption of 3%Ga ZSM-5 Si/Al 25

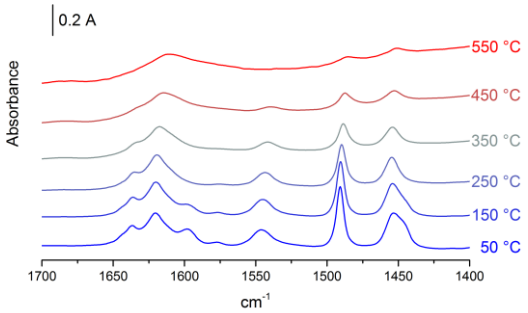

D 4 IR-spectra on Pyridine desorption of 4.5%Ga ZSM-5 Si/Al 25